

**NASA TECHNICAL NOTE**



**NASA TN D-2018**

*C.1*

LOAN COPY: RETUF  
AFWL (WLL—)  
KIRTLAND AFB, NM



NASA TN D-2018

**ANALYSIS OF JET-PLUMING INTERFERENCE BY  
COMPUTER SIMULATION OF MEASURED FLIGHT  
MOTIONS OF TWO RAM A FOURTH STAGES**

*by William F. Hinson and Sherwood Hoffman*

*Langley Research Center*

*Langley Station, Hampton, Va.*



TECHNICAL NOTE D-2018

ANALYSIS OF JET-PLUMING INTERFERENCE  
BY COMPUTER SIMULATION OF MEASURED FLIGHT MOTIONS  
OF TWO RAM A FOURTH STAGES

By William F. Hinson and Sherwood Hoffman

Langley Research Center  
Langley Station, Hampton, Va.

NATIONAL AERONAUTICS AND SPACE ADMINISTRATION

NATIONAL AERONAUTICS AND SPACE ADMINISTRATION

---

TECHNICAL NOTE D-2017

---

FLIGHT TEST AND ANALYSIS OF THE ROLLING MOTIONS  
OF A  $79^\circ$  CLIPPED DELTA CONFIGURATION WITH  
WING-TIP FINS AT SUPERSONIC SPEEDS

By James L. Raper

SUMMARY

A free-flight investigation was conducted to determine the aerodynamic characteristics and motions of a rocket-boosted model of a simplified hypersonic glider configuration with wing-tip fins and a blunt base through a Mach number range extending up to 4.4. The model was statically and dynamically stable at small angles of attack and experienced coupled motions when pitched to an angle of attack of about  $12^\circ$ . The addition of the wing-tip fins resulted in no improvement of the vehicle motions compared with the same vehicle with no fins.

In general, the coupled motions experienced by the model were simulated by the use of the equations of motion for five degrees of freedom. The analog study showed that the rate of change of effective-dihedral derivative with change in angle of attack was a significant cross-coupling derivative for the configuration studied and should be considered for flight prediction of the motions for configurations which are highly swept and have the mass concentrated along the longitudinal axis. An analytical solution for a simplified three-degree-of-freedom set of equations yielded results that compared satisfactorily with the flight records of rolling velocity and yielded a rolling velocity parameter which affected the type of rolling motion experienced. The appendix presents the analytical solution.

INTRODUCTION

The current interest in highly swept, delta wing configurations for high-speed reentry and manned orbital flight has prompted a free-flight investigation to determine the aerodynamic characteristics and dynamic behavior of several research models with these general characteristics. Reference 1 presents the results of one such test and shows that the model angular velocities became large and erratic following a disturbance. The rolling velocities were of particular interest, with periodic positive and negative values along with short-period sinusoidal-like peak-magnitude variations of 35 radians per second being experienced. Electronic analog motion simulation showed that the primary reason for

this behavior was the concentration of mass along the axis of symmetry, the low roll inertia, and the large increase in rolling moment due to sideslip with increasing angle of attack.

The object of this investigation is to present the dynamic behavior of a delta wing configuration which is the same as that of reference 1, except for the addition of wing-tip fins which were added with the idea of increasing directional stability, of reducing coupling forces, and hence, it was thought, of decreasing the roll rates and accelerations.

The model was flight tested at the NASA Wallops Station over a Mach number range from 4.4 to approximately 1.5 with corresponding Reynolds numbers, based on wing mean aerodynamic chord, of  $42.5 \times 10^6$  and  $0.7 \times 10^6$ . Pulse rockets were used to disturb the model in pitch to an angle of attack of about  $12^\circ$ , and a 10-channel telemeter was used to transmit continuous acceleration and pressure data to ground receiving stations.

Aerodynamic coefficients based on accelerations of the center of gravity are presented. With the use of five-degree-of-freedom equations of motion, an analysis of the rolling motions was made by comparing the free-flight data with analog runs for similar altitude and aerodynamic-coefficient conditions. In addition, an analytical solution of a simplified set of three-degree-of-freedom equations of motion were used to predict rolling motions.

#### SYMBOLS

The basic data in this report are presented with respect to an axis system originating at the 54.3-percent station on the longitudinal axis of the rocket model. (See fig. 1.)

$a_{L, cg}$	longitudinal accelerometer reading referenced to center of gravity, g units
$a_{L, Hi}$	high-range longitudinal accelerometer reading, positive in positive x-direction, g units
$a_{L, Lo}$	low-range longitudinal accelerometer reading, positive in positive x-direction, g units
$a_{N, cg}$	normal accelerometer reading referenced to center of gravity, g units
$a_{N, n}$	normal accelerometer reading at nose location, positive in negative z-direction, g units
$a_{N, t}$	normal accelerometer reading at tail location, positive in negative z-direction, g units
$a_Y$	lateral accelerometer reading, positive in positive y-direction, g units

$a_{Y, cg}$	lateral accelerometer reading referenced to center of gravity, g units
$b$	wing span, 1.77 ft
$C_D$	drag coefficient, $\frac{\text{Drag}}{q_\infty S}$
$C_L$	lift coefficient, $C_L \approx C_N \cos \alpha$ , $\frac{\text{Lift}}{q_\infty S}$
$C_{L_\alpha}$	lift-coefficient derivative, $\frac{\partial C_L}{\partial \alpha}$ , per radian
$C_l$	rolling-moment coefficient, $\frac{\text{Rolling moment}}{q_\infty S b}$
$C_{l_p}$	damping-in-roll derivative, $\frac{\partial C_l}{\partial \left(\frac{pb}{2V}\right)}$ , per radian
$C_{l_r}$	rate of change of rolling-moment coefficient with change in yawing angular velocity factor, $\frac{\partial C_l}{\partial \left(\frac{rb}{2V}\right)}$ , per radian
$C_{l_\beta}$	effective-dihedral derivative, $\frac{\partial C_l}{\partial \beta}$ , per radian
$C_{l_{\beta\alpha}}$	rate of change of effective-dihedral derivative with change in angle of attack, $\frac{\partial C_{l_\beta}}{\partial \alpha}$ , per square radian
$C_m$	pitching-moment coefficient, $\frac{\text{Pitching moment}}{q_\infty S \bar{c}}$
$C_{m_q}$	rate of change of pitching-moment coefficient with pitching angular velocity parameter, $\frac{\partial C_m}{\partial \left(\frac{q\bar{c}}{2V}\right)}$ , per radian
$C_{m_\alpha}$	static stability derivative, $\frac{\partial C_m}{\partial \alpha}$ , per radian
$C_{m_{\dot{\alpha}}}$	rate of change of pitching-moment coefficient with rate of change of angle-of-attack parameter, $\frac{\partial C_m}{\partial \left(\frac{\dot{\alpha}\bar{c}}{2V}\right)}$ , per radian

$C_{m\beta}$	rate of change of pitching-moment coefficient with angle of sideslip, $\frac{\partial C_m}{\partial \beta}$ , per radian
$C_N$	normal-force coefficient, $\frac{\text{Normal force}}{q_\infty S}$
$C_{N\alpha}$	normal-force-coefficient derivative, $\frac{\partial C_N}{\partial \alpha}$ , per radian
$C_n$	yawing-moment coefficient, $\frac{\text{Yawing moment}}{q_\infty S b}$
$C_{np}$	rate of change of yawing-moment coefficient with rolling angular velocity parameter, $\frac{\partial C_n}{\partial \left(\frac{pb}{2V}\right)}$ , per radian
$C_{nr}$	rate of change of yawing-moment coefficient with yawing angular velocity parameter, $\frac{\partial C_n}{\partial \left(\frac{rb}{2V}\right)}$ , per radian
$C_{n\beta}$	directional-stability derivative, $\frac{\partial C_n}{\partial \beta}$ , per radian
$C_{n\dot{\beta}}$	rate of change of yawing-moment coefficient with rate of change of angle-of-sideslip parameter, $\frac{\partial C_n}{\partial \left(\frac{\dot{\beta} b}{2V}\right)}$ , per radian
$C_o = -\frac{q_\infty S b}{I_X} C_{l\beta\alpha} \sigma_o^2$	
$C_X$	axial-force coefficient, positive in positive x-direction, $\frac{\text{Axial force}}{q_\infty S}$
$C_Y$	lateral-force coefficient, $\frac{\text{Lateral force}}{q_\infty S}$
$C_{Yr}$	rate of change of side-force coefficient with angular velocity factor in yaw, $\frac{\partial C_Y}{\partial \left(\frac{rb}{2V}\right)}$ , per radian
$C_{Y\beta}$	lateral-force-coefficient derivative, $\frac{\partial C_Y}{\partial \beta}$ , per radian

$\bar{c}$	wing mean aerodynamic chord, 3.83 ft
F,K	incomplete and complete elliptic functions of first kind
g	acceleration due to gravity, 32.2 ft/sec <sup>2</sup>
h	model altitude, ft
I <sub>X</sub>	mass moment of inertia in roll, (slugs)(sq ft)
I <sub>Y</sub>	mass moment of inertia in pitch, (slugs)(sq ft)
I <sub>Z</sub>	mass moment of inertia in yaw, (slugs)(sq ft)
k	critical roll-rate parameter (eqs. (A14) and (A23))
l	reference length, ft
M	Mach number
m	model reference mass, W/g, slugs
p	rolling angular velocity, radians/sec
p <sub>b</sub>	base pressure, lb/sq in.
p <sub>o</sub>	total pressure, measured at nose stagnation point, lb/sq in.
p <sub>∞</sub>	free-stream pressure, lb/sq in.
q	pitching angular velocity, radians/sec
q <sub>∞</sub>	free-stream dynamic pressure, $\frac{\rho V^2}{2}$ , lb/sq ft
R	Reynolds number, based on wing mean aerodynamic chord (3.83 ft), $\frac{\rho V l}{\mu}$
r	yawing angular velocity, radians/sec
S	wing reference area, 5.87 sq ft
t	time, sec
V	velocity, ft/sec
W	model weight, lb
X,Y,Z	fixed body-axis system
x,y,z	distances measured along the X-, Y-, and Z-axes

$\alpha$	angle of attack, radians
$\beta$	angle of sideslip, radians
$\gamma$	flight-path angle referenced to local horizontal, deg
$\mu$	free-stream coefficient of viscosity, lb-sec/sq ft
$\rho$	free-stream density, slugs/cu ft

$$\sigma_0 = \sqrt{\alpha_0^2 + \beta_0^2}$$

$\phi$  angle of roll, radians

$$\psi = \sin^{-1}(k \sin \phi)$$

Subscripts:

min minimum value

max maximum value

o initial condition

A dot (·) over a symbol denotes a first derivative with respect to time, and double dots (··) over a symbol denote a second derivative with respect to time. A bar (¯) indicates an angle normalized with respect to  $\sigma_0$ .

## MODEL AND INSTRUMENTATION

### Model

A dimensional drawing of the rocket-boosted model is shown in figure 2. The reference areas and lengths and physical characteristics of the model are given in table I. Photographs of the model are presented in figure 3, and a photograph of the model and booster in launch position is shown in figure 4.

The model had planar symmetry in the horizontal and vertical planes, sharp leading edges, and a blunt trailing edge. The planform of the basic body was a 78.87° sweptback clipped delta surface with streamwise tips, aspect ratio of 0.53, and a taper ratio of 0.191. The wing-tip fins were clipped delta surfaces swept back 70°. The vertical tail had a sweepback angle of 76°. The planar surfaces of the model were not properly aligned in some instances because of tolerances of construction giving rise to slight aerodynamic asymmetries. A detailed description is presented in table I and figure 2 of the physical and mass characteristics of the complete model and of each component. For all practical purposes, the mass balance of the model was such that the principal axes were coincident with the body axes of symmetry.



## Instrumentation

The rocket-boosted model was equipped with a 10-channel telemeter which continuously transmitted information concerning longitudinal, transverse, and normal acceleration; angular acceleration in pitch and yaw; angular velocity in roll; and total and base pressures. There were two longitudinal accelerometers, one with a  $g$ -unit range from 1 to -12 and one with a  $g$ -unit range from 1 to -2. There were also two normal accelerometers, one mounted in the nose section of the model, and the other mounted in the rear of the model. The base pressure data represented an average over the semispan of the blunt trailing edge of the model as obtained by a manifolded tube, as shown in figures 2 and 3(b). The locations of the instruments with respect to the center of gravity are given in table II.

The data accuracy of the 10 instruments installed in the rocket-propelled model was approximately  $\pm 5$  percent of the calibrated scale of each instrument. The error in the aerodynamic coefficients was dependent on the free-stream dynamic pressure, which had a possible variation of 25 percent, on velocity, which had possible variations of  $\pm 100$  feet per second, and on density, which had possible variations of  $\pm 5$  percent.

## TESTS

Figure 4 is a photograph of the rocket model and launch vehicle elevated on the launcher prior to firing at the NASA Wallops Station. The three-stage launch vehicle consisted of an Honest John rocket with four standard 12-square-foot trapezoidal fins for a ground-fired first stage; a Nike M5 rocket motor with four standard 5-square-foot trapezoidal fins for a delayed, ground-fired second stage; and a Nike with four standard 5-square-foot  $4^\circ$  wedge fins for a ground initiated, timer-fired third stage.

A small pancake rocket motor was installed in the base of the model behind the blowout diaphragm (see fig. 3(b)) and was programed to separate the model from the burned-out third-stage Nike. Preflight calculations of the relative decelerations of the burned-out third-stage Nike and the model, based on drag-weight ratios, indicated the need for an additional separation force in order to prevent collision after separation. In order that this requirement be satisfied, two 3.25-inch Mk 7 rocket motors were strapped in reverse thrust position to the forward end of the third-stage Nike, as shown in figure 4. The nozzles of the two rocket motors were canted out  $20^\circ$  with respect to the center line of the third stage and were plugged and sealed to protect the grain and igniters from aerodynamic heating during the boosted portion of the flight.

Two pulse rockets with 27 pound-seconds of impulse (burning time 0.05 second) were located in the nose section of the model (see fig. 2) and so oriented that the direction of thrust was in the positive and negative  $z$ -directions. Approximate calculations prior to the free-flight test for which two-degree-of-freedom pitch-plane dynamics and aerodynamic coefficients from reference 2 were used indicated that the maximum disturbance in the pitch plane alone would be about  $12^\circ$ .

Continuous flight-path data were obtained by tracking the model with three radar sets: an AN/FPS-16, an SCR-584, and an SCR-584 Model II. Atmospheric conditions were obtained from a Rawinsonde balloon which was released prior to launch. Mach number and dynamic pressure were determined from the total pressure measurements of the model and the ambient pressures and temperatures at corresponding altitudes along the flight path. The error of the most accurate tracking radar set used (AN/FPS-16) was 0.1 mil for the given angular measurement and 50 feet for the given linear measurement.

Data are presented in this report ranging from a Mach number of about 4.4 at an altitude of about 34,000 feet to a Mach number of 1.1 at an altitude of about 108,000 feet. The variation of altitude with Mach number is presented in figure 5. Variations of dynamic pressure and Reynolds number with Mach number are presented in figures 6 and 7, respectively.

Plots of 10 channels of telemeter data, dynamic pressure, and Mach number for three time intervals of the flight test of the model are presented in figure 8. The points were machine plotted from magnetic tape records and show occasional scatter points due to noise. Figure 9 presents an envelope of the variation of maximum roll rates plotted against Mach number for the flight.

## ANALYSIS

### Basic Data Reduction

The measured free-flight linear-acceleration data were corrected to the center of gravity because linear accelerometers which are not mounted on the center of gravity measure not only the translatory accelerations but also the accelerations due to angular velocities and angular accelerations. The following relationships were used to correct the accelerometer readings to the center of gravity:

$$a_{L, cg} = a_{L, Lo} + \frac{1}{g} \left[ x_{aL, Lo} (q^2 + r^2) + y_{aL, Lo} (\dot{r} - pq) - z_{aL, Lo} (\dot{q} + pr) \right] \quad (1)$$

$$a_{Y, cg} = a_{Y} + \frac{1}{g} \left[ y_{aY} (r^2 + p^2) + z_{aY} (\dot{p} - qr) - x_{aY} (\dot{r} + pq) \right] \quad (2)$$

and

$$a_{N, cg} = a_{N, n} + \frac{1}{g} \left[ -z_{aN, n} (p^2 + q^2) - x_{aN, n} (\dot{q} - pr) + y_{aN, n} (\dot{p} + qr) \right] \quad (3)$$

where the distances  $x$ ,  $y$ , and  $z$  from the center of gravity to the individual accelerometer are given in table II. The variations of  $\dot{q}$ ,  $\dot{r}$ , and  $\dot{p}$  were measured directly from the angular accelerometers and the roll gyro, respectively,

and required no corrections. The variations of  $q$  and  $r$  were obtained by integration of  $\dot{q}$  and  $\dot{r}$  over several cycles and by assuming that they varied symmetrically about zero values. The angular acceleration in roll  $\dot{p}$  was obtained by differentiating  $p$  with time.

The values of  $a_{L,Lo}$  and  $a_{N,n}$  were used for determining  $a_{L,cg}$  and  $a_{N,cg}$ , respectively, throughout most of the flight. The values of  $a_{L,Hi}$  were used only at the higher Mach numbers where the deceleration was greater than the range of  $a_{L,Lo}$ ; and  $a_{N,t}$  served only as a check for  $a_{N,cg}$ .

The total force coefficients were determined from the instantaneous values of the translatory accelerations (referenced to the center of gravity) as follows:

$$C_N = \frac{W}{q_\infty S} a_{N,cg} \quad (4)$$

$$-C_X = \frac{W}{q_\infty S} a_{L,cg} \quad (5)$$

and

$$C_Y = \frac{W}{q_\infty S} a_{Y,cg} \quad (6)$$

The total moment coefficients for the rocket model were computed from the instantaneous values of angular acceleration and velocity by using the following expressions:

$$C_m = \frac{I_Y}{q_\infty S \bar{c}} \dot{q} + \left( \frac{I_X - I_Z}{q_\infty S \bar{c}} \right) pr \quad (7)$$

$$C_n = \frac{I_Z}{q_\infty S b} \dot{r} + \left( \frac{I_Y - I_X}{q_\infty S b} \right) pq \quad (8)$$

and

$$C_l = \frac{I_X}{q_\infty S b} \dot{p} + \left( \frac{I_Z - I_Y}{q_\infty S b} \right) qr \quad (9)$$

## Analog Simulation

An analog simulation analysis similar to that of references 1 and 3 was used to study rolling velocities of the model near Mach numbers 4 and 2. There were three reasons for using the analog computer for motion simulation: (1) the vehicle aerodynamics were known to be nonlinear with angle of attack or yaw; (2) the lateral and longitudinal aerodynamics were coupled by the rolling velocity; and, (3) the vehicle motions were not symmetrical. The equation associated with the drag force was omitted since the velocity of the model was nearly constant through the time intervals studied. The cross-product inertia terms have been omitted from the equations because the principal axes coincided with the body axes. The equations of motion were written for the body-axis system and are as follows:

Normal force:

$$\dot{\alpha} = q - \beta p - \frac{q_{\infty} S}{mV} C_{L_{\alpha}} \alpha \quad (10)$$

Side force:

$$\dot{\beta} = -r + \alpha p + \frac{q_{\infty} S}{mV} C_{Y_{\beta}} \beta \quad (11)$$

Rolling moment:

$$\dot{p} = \left( \frac{I_Y - I_Z}{I_X} \right) qr + \frac{q_{\infty} S b}{I_X} (C_{l_{\beta}} \beta + C_{l_{\beta \alpha}} \beta \alpha) + \frac{q_{\infty} S b^2}{2VI_X} (C_{l_p} p + C_{l_r} r) \quad (12)$$

Pitching moment:

$$\dot{q} = \left( \frac{I_Z - I_X}{I_Y} \right) pr + \frac{q_{\infty} S \bar{c}}{I_Y} C_{m_{\alpha}} \alpha + \frac{q_{\infty} S \bar{c}^2}{2VI_Y} (C_{m_q} q + C_{m_{\dot{\alpha}}} \dot{\alpha}) \quad (13)$$

Yawing moment:

$$\dot{r} = \left( \frac{I_X - I_Y}{I_Z} \right) pq + \frac{q_{\infty} S b}{I_Z} C_{n_{\beta}} \beta + \frac{q_{\infty} S b^2}{2VI_Z} (C_{n_r} r + C_{n_{\dot{\beta}}} \dot{\beta} + C_{n_p} p) \quad (14)$$

The body was assumed rigid and the gravity terms were omitted from the equations. Certain aerodynamic terms, such as  $C_{m_{\beta}}$  and  $C_{Y_r}$ , were omitted from equations (10) to (14), inasmuch as their effect on the motions was considered to be negligible. In the analog study it was assumed that  $\dot{\beta} = -r$  in equation (14), thus allowing some simplification in the last term.

The equations of motion for five degrees of freedom were used at  $M = 4$  and  $M = 2$ . The static stability derivatives from reference 5 were used in the analog study at  $M = 2$  after they were transferred from the reference point of reference 5 (66.6 percent of the theoretical body length behind the theoretical apex) to the center of gravity of the vehicle. The damping-in-pitch coefficients  $C_{m_q}$

and  $C_{m\dot{\alpha}}$  were initially calculated from linearized theory (refs. 6 and 7), but their values were lowered when they were found to be excessive for an accurate simulation of the motions.

The damping-in-yaw coefficients  $C_{n_r}$  and  $C_{n\dot{\beta}}$  were also calculated in a manner similar to that for pitch, with the assumption that all damping was due to the wing-tip fins and vertical tail. The value for  $C_{l_p}$  was estimated from reference 8, and values for  $C_{l_r}$  and  $C_{n_p}$  were estimated from lifting-line theory. Table III presents values for all the derivatives used. It should be noted that two slopes were used to approximate  $C_{Y\beta}$ ,  $C_{n\beta}$ , and  $C_{l\beta\alpha}$  because they were non-linear with  $\beta$  and/or  $\alpha$ . (These slopes were obtained from wind-tunnel tests of ref. 5.) The initial conditions for the equations of motion were obtained at a given time in the free-flight record. Initial values of  $\alpha$  and  $\beta$  were found by solving the equations of motion. The initial conditions for the analog investigations made for  $M = 4$  and  $M = 2$  are given in table IV.

Because of the large predominating effect of  $C_{l\beta\alpha}$  on the motions, a highly simplified motion study was made with the use of the following three-degree-of-freedom equations of motion:

$$\dot{\alpha} = -\beta p \quad (15)$$

$$\dot{\beta} = \alpha p \quad (16)$$

$$\dot{p} = \frac{q_{\infty} S b}{I_X} C_{l\beta\alpha} \beta \alpha \quad (17)$$

An analytical solution for this simplified set of equations is included in the appendix.

## RESULTS AND DISCUSSION

### Basic Data

One of the purposes of the flight test presented in this paper was to determine if the roll rates and accelerations of the basic vehicle could be decreased by the addition of two wing-tip fins. Reference 5 presents longitudinal and lateral stability data for the model of reference 1 (the basic model) at Mach numbers of 1.41 and 2.01 and for the model of this report at a Mach number of 2.01. The Reynolds numbers of these wind-tunnel tests are given in figure 7. As shown in reference 5, the vehicle with wing-tip fins was statically stable at a Mach number of 2.01. As a result of adding wing-tip fins to the basic configuration, wind-tunnel data (ref. 4) at  $M = 2.01$  and  $\alpha = 4^\circ$  show that  $C_{n\beta}$  was increased from 0.0005 to 0.0022 per degree,  $C_{l\beta\alpha}$  was decreased from -0.0012 to -0.0014,

$C_{Y_\beta}$  was decreased from -0.0020 to -0.0045, and  $C_m$  was decreased from 0.0025 to -0.0010, all of which were referenced to the 66.6 percent longitudinal station behind the theoretical apex and/or the wing mean aerodynamic chord. Even though the directional and longitudinal stability was increased, a comparison of the roll-rate histories for the present test and those of reference 1 shows similar types of oscillations for both models. The reason for this result is that the addition of the wing-tip fins did not result in a decrease in  $C_{l_{\beta\alpha}}$ .

Figure 8(a) shows the time interval from 23.5 to 24.5 seconds, which begins just after model separation (23.48 seconds) and includes the period during which the first pulse-rocket ignition occurred (23.52 seconds). This figure indicates that the model experienced oscillations of large amplitude, due to the pulse rocket, which were coupled in pitch and yaw. The roll rate oscillated about zero through large amplitudes during and immediately after pulse-rocket ignition and then steadily increased to a large positive amplitude of approximately 35 radians per second. The second pulse rocket was ignited at 27.01 seconds. Figure 8(b) presents data from 28.5 to 29.5 seconds and shows the sinusoidal oscillation of the model in roll, pitch, and yaw. Figure 8(c) presents data from 38.6 to 39.6 seconds for  $M = 2$  after ignition of the second pulse rocket. In general, the motions of the model were coupled, and the roll rate over some intervals was unsteady and varied randomly from positive roll oscillations through roll reversals.

Vehicle oscillation about the stability boundary was considered as a possible cause of the coupled motions. By using the methods of references 4 and 9, it is possible to superimpose a region of roll divergence for steady roll rates on the curve of figure 9. The figure indicates that from  $M = 4.2$  to  $M = 3.7$  the roll rates are not in the regions of divergence; however, at lower Mach numbers the roll rates cross back and forth over the boundaries of divergence. It should be noted that the moments are coupled prior to encountering the regions of divergence, which indicates that the cause of the coupling is purely aerodynamic. It should also be noted that the boundaries were derived for constant roll rates and linear equations of motion, which do not account for the second-order effects such as that of  $C_{l_{\beta\alpha}}$ , and, consequently, the boundaries may not be applicable for this flight condition.

The variation of the total force and moment coefficients with time is presented in figures 10 to 13 for four time increments. The time increments were picked to show variation in aerodynamics (1) after model separation and during first pulse-rocket ignition at  $M \approx 4.1$ ; (2) after first pulse-rocket disturbance at  $M \approx 3.9$ ; (3) after second pulse-rocket disturbance at  $M = 3.1$ ; and (4) after second pulse-rocket disturbance at  $M \approx 2.1$ . Parts (a) and (b) of these figures are the longitudinal coefficients, total normal force and total pitching moment, respectively. Parts (e) and (f) are the directional coefficients, total side force and total yawing moment, respectively; parts (c) and (g) are total axial force and total rolling-moment coefficients, respectively. Parts (d) and (h) of figures 10 to 13 are variations of total pitching moment plotted against total normal-force coefficient and of total yawing moment plotted against total side-force coefficient, respectively. A line representing the approximate slope of the data has been drawn through some of the curves indicating static stability as shown by

The result of reducing the normal force or flare-restoring force is indicated in the nonlinear  $C_m$  and  $x_{cp}$  curves O-A-B'-G' of figures 13(b) and (c). These curves indicate that the vehicle is statically unstable up to an angle of attack of  $2^\circ$  and stable for larger angles of attack. The center-of-pressure curve O-A-B'-G' indicates that the  $x_{cp}$  moves from that of the nose cone rearward to approximately 2 feet aft of the center of gravity at  $\eta = 5^\circ$  where the free-stream flow is fully attached to the flare. Although the flight measurements and simulations presented for vehicle 1 are the angular motions in the pitch plane only, motions in the yaw plane are essentially similar except for a  $90^\circ$  phase lag.

A thrust misalignment of  $0.1^\circ$  in the XZ-plane did not alter the nature of the simulation pattern. This was primarily due to the spin of the vehicle. Jet-damping effects were small, as can be seen from the small attenuation (about  $1^\circ$ ) of the low-frequency mode or motion envelope of the flight and from simulated data of figures 15(a) and (b).

#### Vehicle 2 - Thrusting

Vehicle 2 was instrumented to provide angle-of-incidence measurements in both pitch and yaw planes. These data are compared in figure 16 with the best simulation run. These simulated runs were obtained from the same O-A-B'-G' curves (fig. 13) as were used for vehicle 1. It should be noted that vehicle 2 had a longer cylindrical center body (4.2 in. longer), but the change in overall fineness ratio was estimated to have a negligible effect on the aerodynamic characteristics.

The overall amplitudes and frequencies of the flight and simulated body motions are in good agreement. For the cases shown in figures 16(b) and (d), jet-pluming termination was assumed shortly after motor tail-off started (approximately 57.3 sec). Again,  $p_j/p_\infty$  is decreasing very rapidly to zero.

Data for vehicle 2 indicate a large initial disturbance which resulted in a maximum angle of attack of about  $15^\circ$ . The vehicle motion damped to about an angle of attack of  $6^\circ$  at burnout. Since aerodynamic damping was negligible, it appears that jet damping and flare-restoring moment reduced the amplitude of oscillation to half in about 1.5 seconds in both flight and simulated histories. From the simulation analysis, it appears that about 75 percent of the attenuation is due to jet damping.

The small differences between the flight and simulated data may be due to possible errors in the low flight dynamic-pressure measurements, errors due to thrust (since the nominal thrust curve was used instead of the actual flight thrusts), small errors in the rolling velocity, and errors in inertia. A study of the equations of motion used in the simulation analysis indicates that the aforementioned effects on the motions would be small compared with the nonlinear aerodynamic inputs employed in this study.

Cross plots of  $\alpha$  and  $\beta$  are compared in figure 17. This comparison gives a more realistic picture of the agreement between the best simulated motions and the flight data. It appears that use of the nonlinear aerodynamic curves O-A-B'-G'

(fig. 13) provides a close simulation of the epicycloid motions of the flight as well as the resultant angle of attack. The inside loops indicate that the model was rolling above aerodynamic resonance (see ref. 12).

#### Vehicle 2 - Coast

The curves in figure 18 show good agreement between the flight and digital computer motions, and fair agreement with the computed motions made by using the linearized theory solutions of reference 12. Both simulations shown are based on the same initial conditions at the beginning of the coast-flight phase (see table II). It should be noted that the machine-computed motor-burnout conditions differed slightly from those of the flight measurements, and that a new set of initial conditions was computed for use in the coast simulations based on the flight measurements. The linearized solution consists of two rotating vectors of equal amplitudes - one rotating at the nutational frequency and the other at the precessional frequency. Using average values of normal-force slope and pitching-moment slope between  $0^\circ$  and  $5^\circ$  angle of attack, the linear theory gives a rapid description of the motions for approximately constant velocity and dynamic pressure. In figure 18 only the linearized theory solution for the  $\alpha$ -plane has been presented. As stated previously, the motion in the  $\beta$ -plane is essentially the same as  $\alpha$  except for a phase lag of  $90^\circ$ .

#### CONCLUDING REMARKS

The effect of jet pluming on the aerodynamics of two RAM A vehicles has been analyzed by comparing the aerodynamic coefficients required (in a six-degree-of-freedom computer program) to simulate the angular flight motions measured both with and without jet-pluming interference. Nonlinear aerodynamics, based on Newtonian theory and wind-tunnel data, were employed for the analysis. The following observations were made:

The frequencies and amplitudes of the measured angular motions during jet-pluming flight were simulated by using the estimated nonlinear aerodynamic forces and moments along with nominal rocket-motor characteristics.

From the analysis it is evident that boundary-layer separation induced by jet-pluming interference caused a marked reduction in flare effectiveness which resulted in a significant loss of normal force and stability at low angles of attack as compared with jet-off conditions. The vehicles were unstable between approximately  $0^\circ$  and  $2^\circ$  angle of attack. As the angle of attack was increased from  $2^\circ$  to  $5^\circ$  the flare became progressively more effective and it appeared that full-flare effectiveness was realized at  $5^\circ$  and larger angles of attack. The interference increased the trim angle of attack from  $0^\circ$  to about  $3.5^\circ$ . Pitching-moment slopes corresponding to these trim angles were -0.33 and -0.66, respectively.



During coasting flight where the aerodynamics were only slightly nonlinear, the observed jet-off motions of the vehicle were simulated as before by using the six-degree-of-freedom digital-computer program. In addition, linearized theory solutions of the equations of motion were found to give a rapid description of the measured vehicle motions during coast.

Langley Research Center,  
National Aeronautics and Space Administration,  
Langley Station, Hampton, Va., August 2, 1963.

## REFERENCES

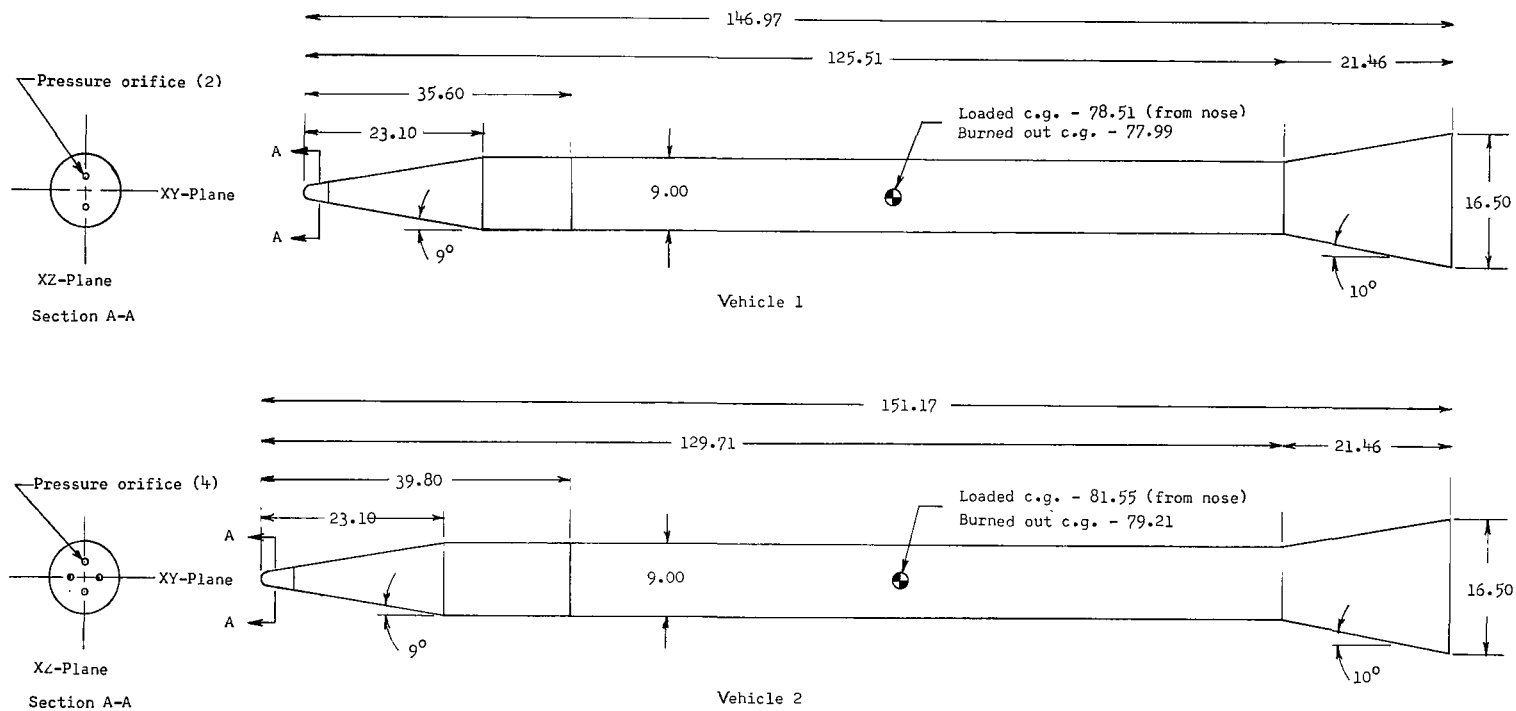
1. Falanga, Ralph A., Hinson, William F., and Crawford, Davis H.: Exploratory Tests of the Effects of Jet Plumes on the Flow Over Cone-Cylinder-Flare Bodies. NASA TN D-1000, 1962.
2. Hinson, William F., and Falanga, Ralph A.: Effect of Jet Pluming on the Static Stability of Cone-Cylinder-Flare Configurations at a Mach Number of 9.65. NASA TN D-1352, 1962.
3. Stalmach, C. J., Jr., and Cooksey, J. M.: Simulation of Rocket Power Effects on Vehicle Stability and Measurements of Aerodynamic Damping in a Hypervelocity Wind Tunnel. IAS Paper No. 62-24, 1962.
4. Fetterman, David E., Jr.: Effects of Simulated Rocket-Jet Exhaust on Stability and Control of a Research-Type Airplane Configuration at a Mach Number of 6.86. NASA TM X-127, 1959.
5. Dryer, Murray, and North, Warren J.: Preliminary Analysis of the Effect of Flow Separation Due to Rocket Jet Pluming on Aircraft Dynamic Stability During Atmospheric Exit. NASA MEMO 4-22-59E, 1959.
6. Levine, Jack: Performance and Some Design Aspects of the Four-Stage Solid-Propellant Rocket Vehicle Used in the RAM A1 Flight Test. NASA TN D-1611, 1963.
7. Sims, Theo E., and Jones, Robert F.: Flight Measurements of VHF Signal Attenuation and Antenna Impedance for the RAM A1 Slender Probe at Velocities up to 17,800 Feet Per Second. NASA TM X-760, 1963.
8. Carter, Howard S., and Wright, Robert L.: Heat Transfer to a Hemispherically Blunted  $9^\circ$  Half-Angle Cone During Free Flight at Mach Numbers Up to 20.8. NASA TM X-908, 1963.
9. Swalley, Frank E.: Measurement of Flow Angularity at Supersonic and Hypersonic Speeds With the Use of a Conical Probe. NASA TN D-959, 1961.
10. Truitt, Robert Wesley: Hypersonic Aerodynamics. The Ronald Press Co., c.1959.
11. Minzner, R. A., Champion, K. S. W., and Pond, H. L.: The ARDC Model Atmosphere, 1959. Air Force Surveys in Geophysics No. 115 (AFCRC-TR-59-267), Air Force Cambridge Res. Center, Aug. 1959.
12. Nelson, Robert L.: The Motions of Rolling Symmetrical Missiles Referred to a Body-Axis System. NACA TN 3737, 1956.
13. Penland, Jim A.: Static Longitudinal Stability of a Missile Configuration With Various Nose Shapes and Flared Afterbodies at a Mach Number of 6.82. NASA TM X-274, 1960.

TABLE I.- MASS CHARACTERISTICS

Vehicle 1			
t, sec	W, lb	I <sub>y</sub> , slug-ft <sup>2</sup>	I <sub>x</sub> , slug-ft <sup>2</sup>
55.91	472.0	135.0	1.43
56.50	375.0	121.0	1.27
57.00	298.0	111.0	1.16
57.50	230.0	104.0	1.06
57.60	219.0	103.0	1.04
57.70	213.0	102.0	1.02
57.90	208.0	100.0	.98
58.30	204.0	97.0	.93
Vehicle 2			
55.73	482.0	160.0	1.25
56.50	355.0	145.0	1.00
57.10	256.0	135.0	.89
57.30	224.0	133.0	.85
57.50	221.0	130.0	.82
57.90	219.0	127.5	.75
58.30	215.0	125.5	.69

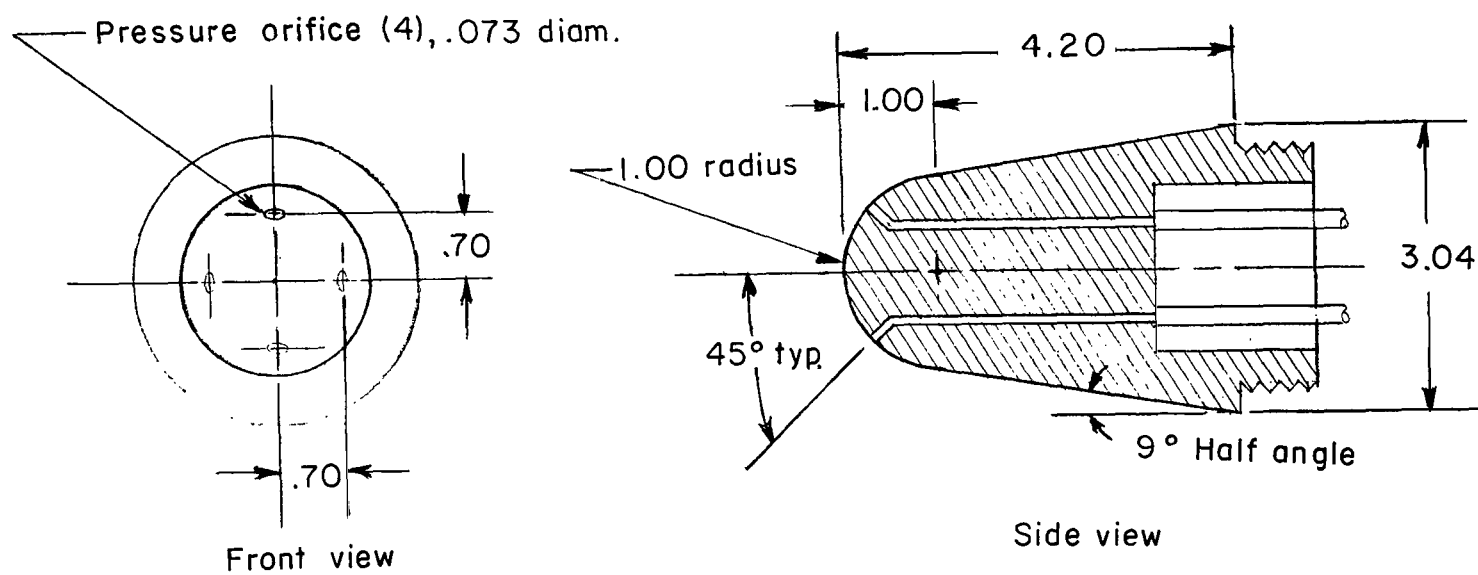
TABLE II.- INITIAL CONDITIONS FOR EQUATIONS OF MOTION

	Vehicle 1	Vehicle 2	
	Thrust	Thrust	Coast
t, sec . . . . .	55.91	55.79	58.3
p, rad/sec . . . . .	-28.4	-24.64	-28.03
q, rad/sec . . . . .	0.17	1.1	0.05
r, rad/sec . . . . .	-0.20	-0.91	0
V <sub>a</sub> , ft/sec . . . . .	11,500	11,500	17,600
h, ft . . . . .	151,000	131,000	154,000
$\alpha$ , deg . . . . .	-1	2	0
$\beta$ , deg . . . . .	1	2	5.5
$\dot{\alpha}$ , rad/sec . . . . .	0.66	1.96	2.73
$\dot{\beta}$ , rad/sec . . . . .	-0.28	-1.77	0
$\phi$ , deg . . . . .	0	0	0
$\theta$ , deg . . . . .	48.4	41.0	43.0
$\psi$ , deg . . . . .	0	0	0
Thrust misalignment in XZ-plane, deg . . .	0.1	0.1	0



(a) General vehicle dimensions.

Figure 1.- Dimensional characteristics of the flight-test vehicles. All dimensions are in inches.



(b) General nose dimensions of vehicle 2.

Figure 1.- Concluded.

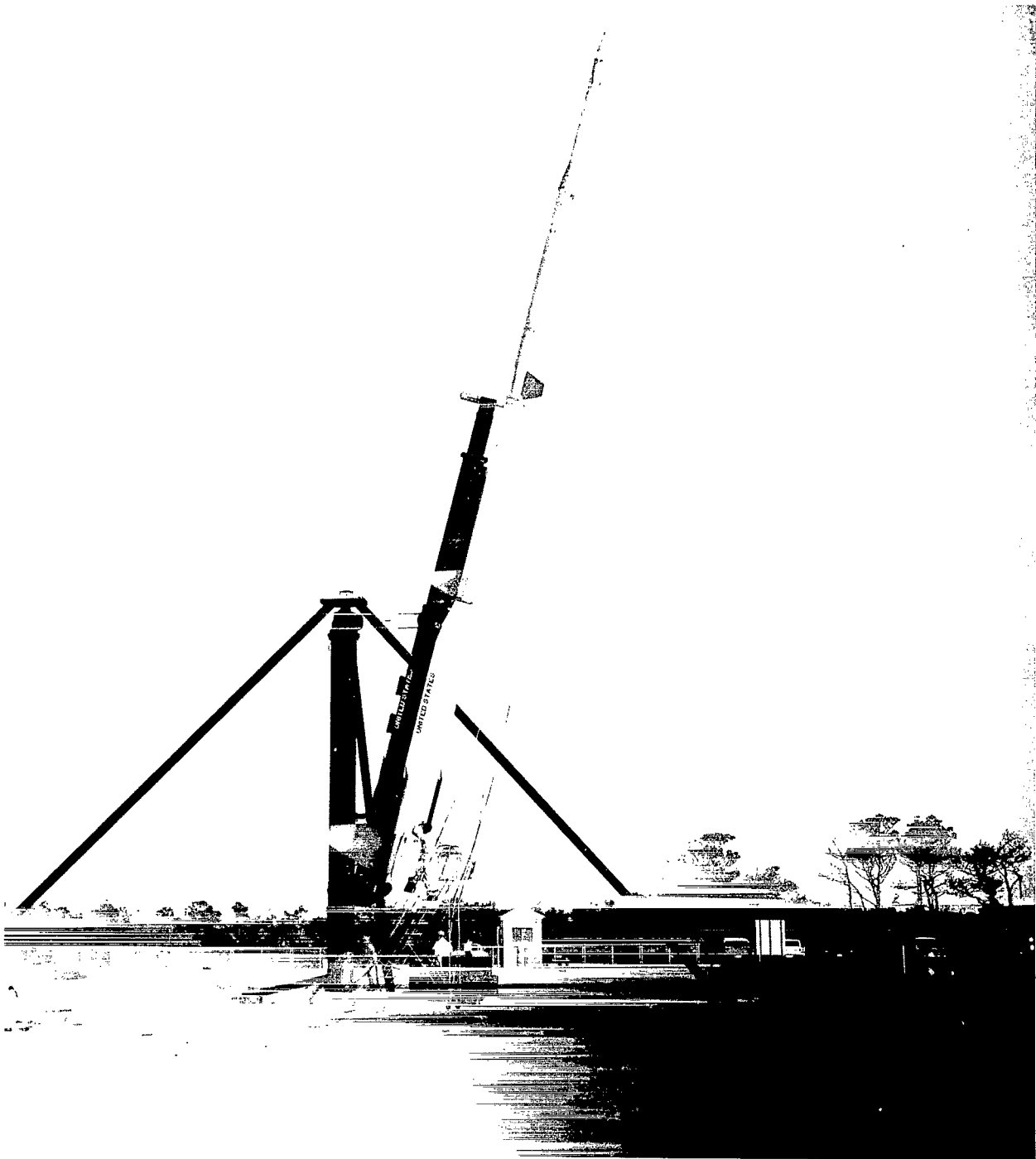


Figure 2.- Photograph of vehicle 1 (RAM A1) and booster system in launch position. L-61-6238

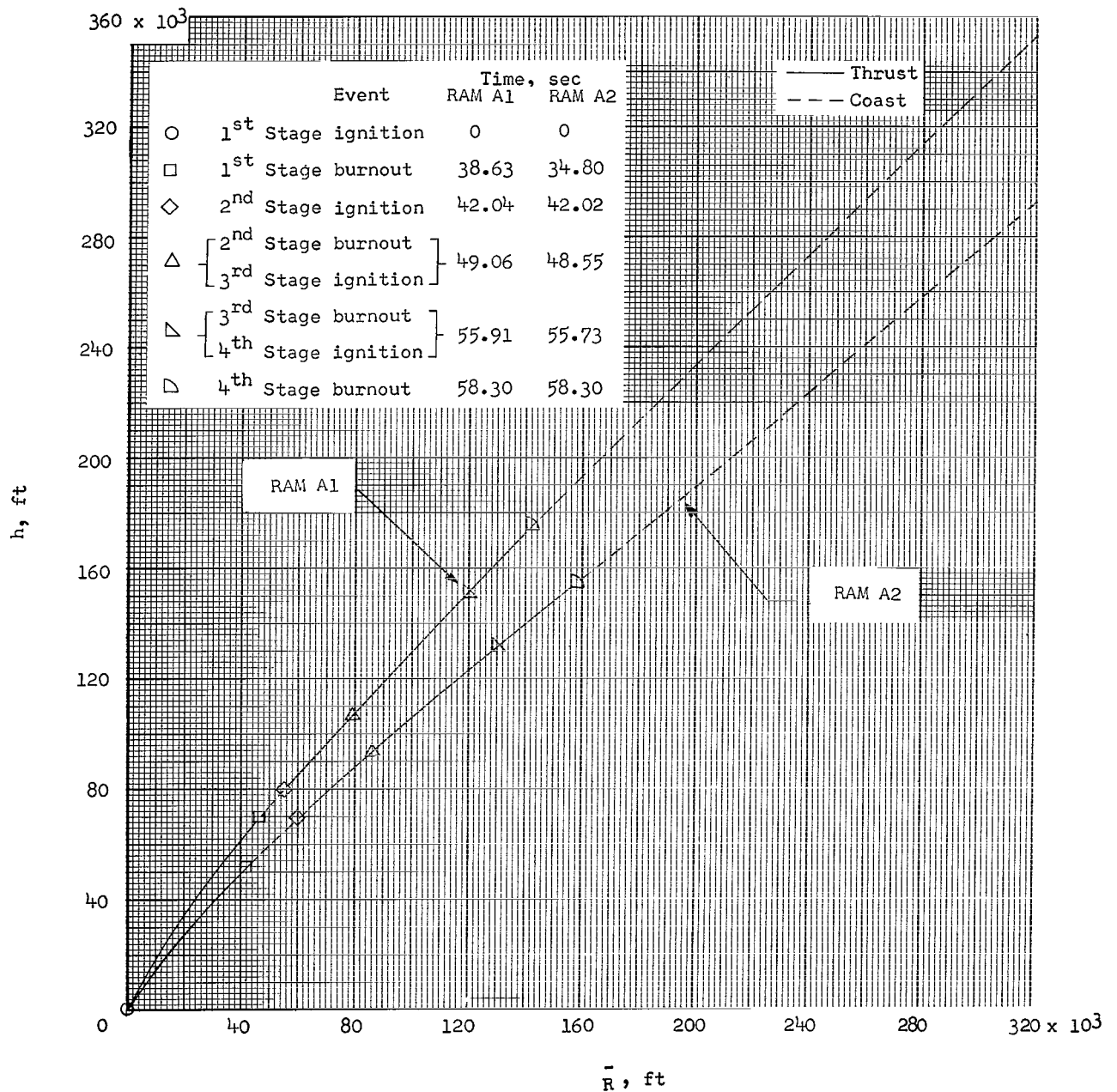
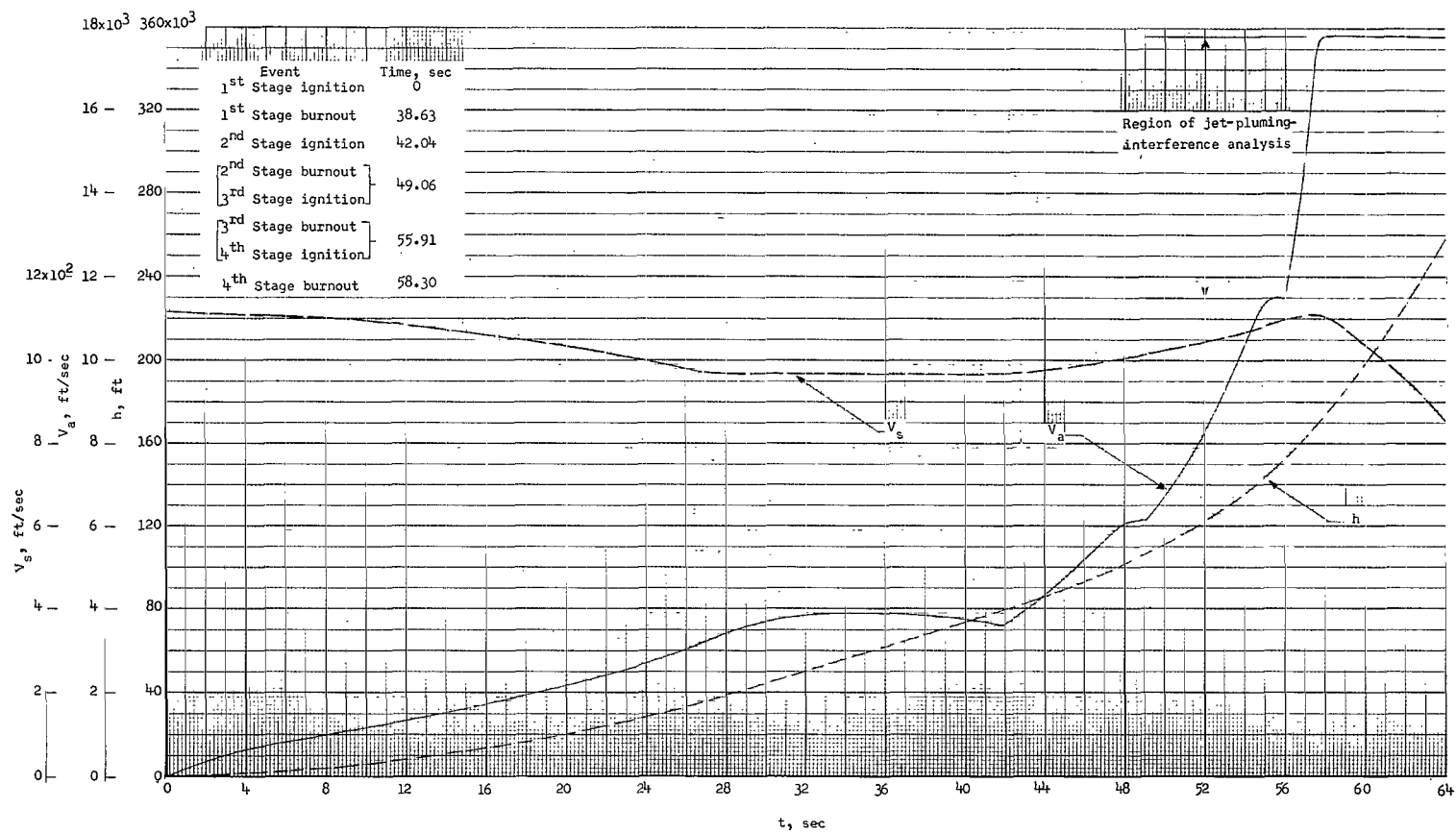


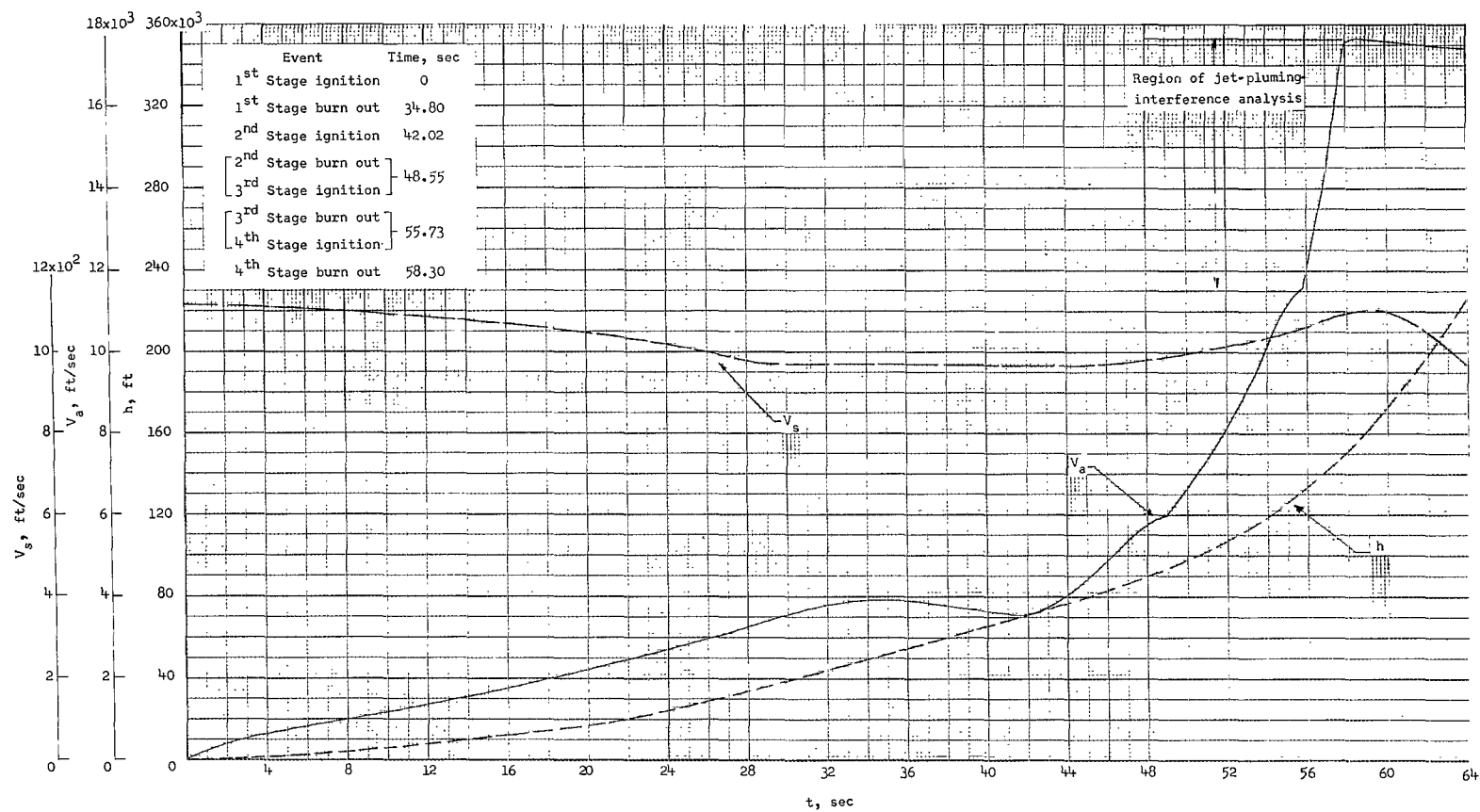
Figure 3.- Variation of altitude with horizontal range.





(a) RAM A1.

Figure 4.- Variation of velocity, altitude, and speed of sound with time.



(b) RAM A2.

Figure 4.- Concluded.

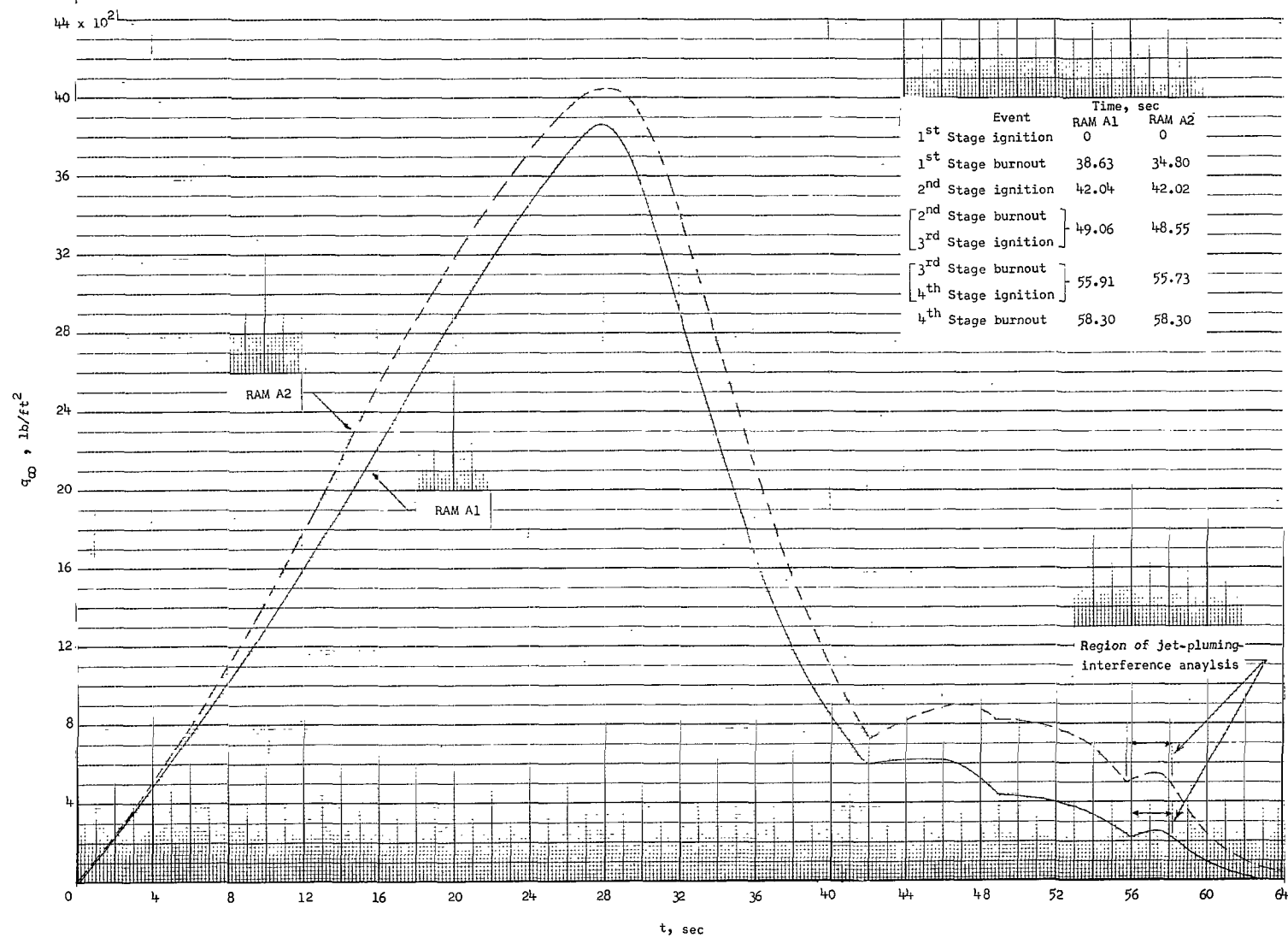


Figure 5.- Variation of free-stream dynamic pressure with time.

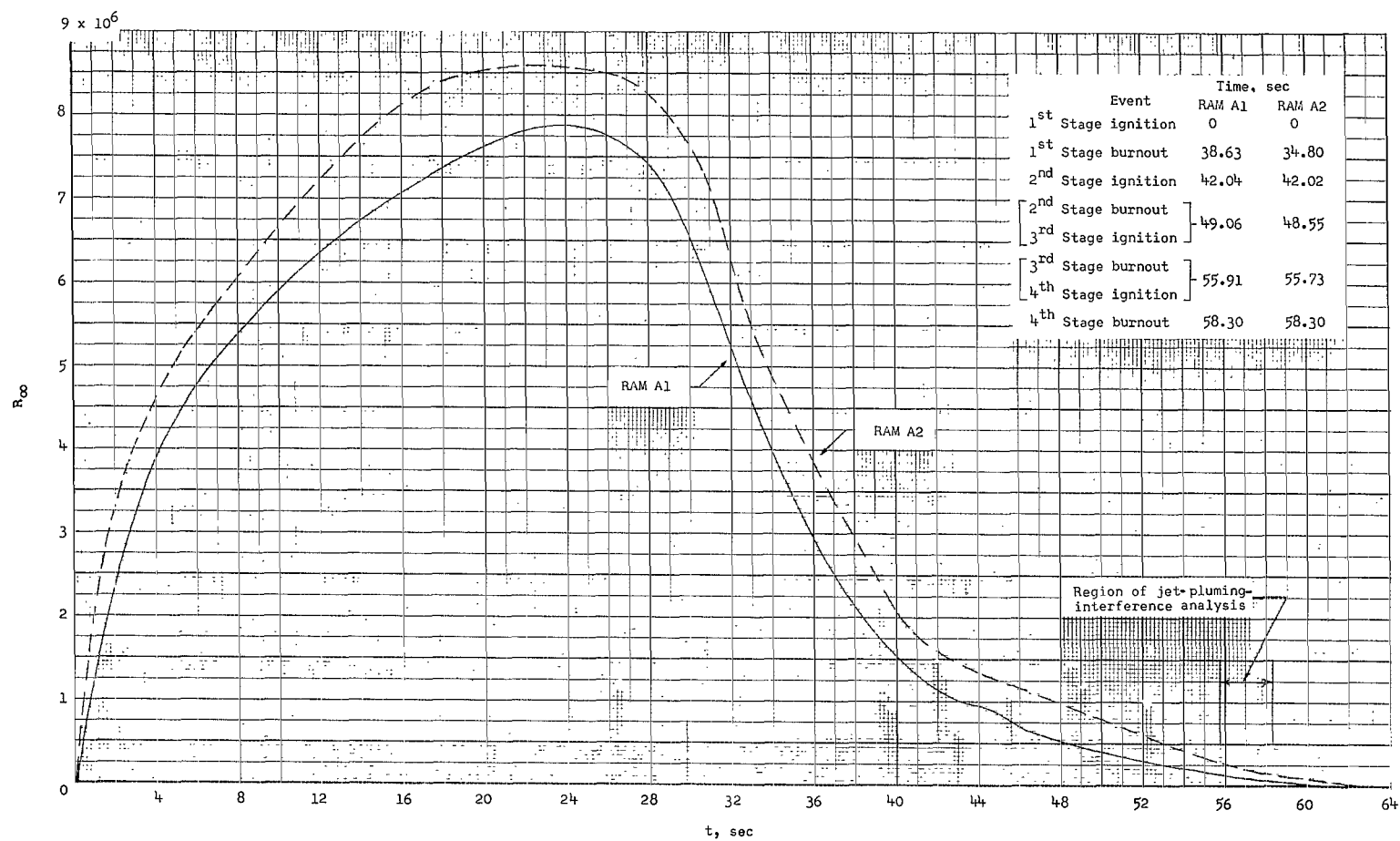


Figure 6.- Variation of free-stream Reynolds number with time.

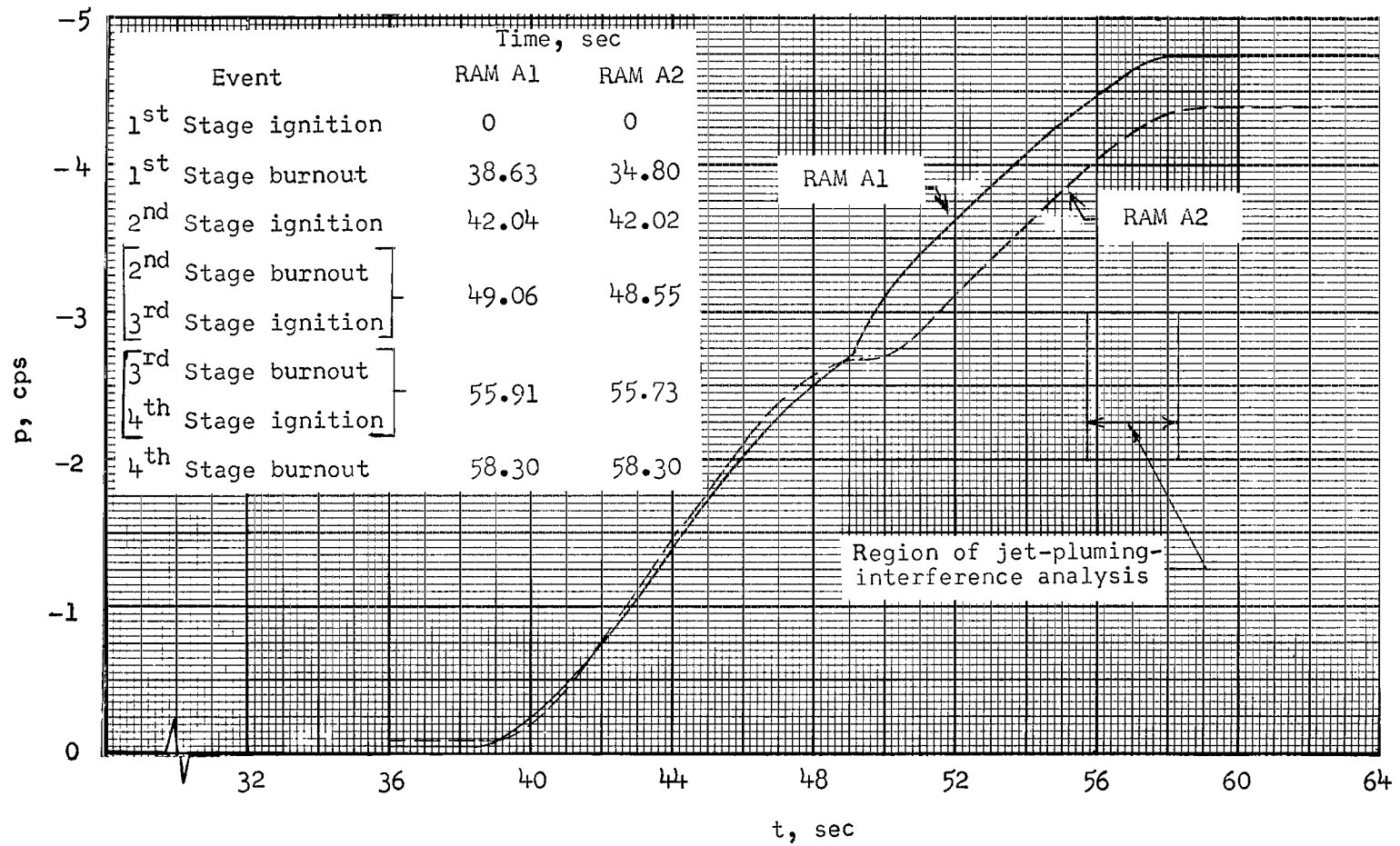
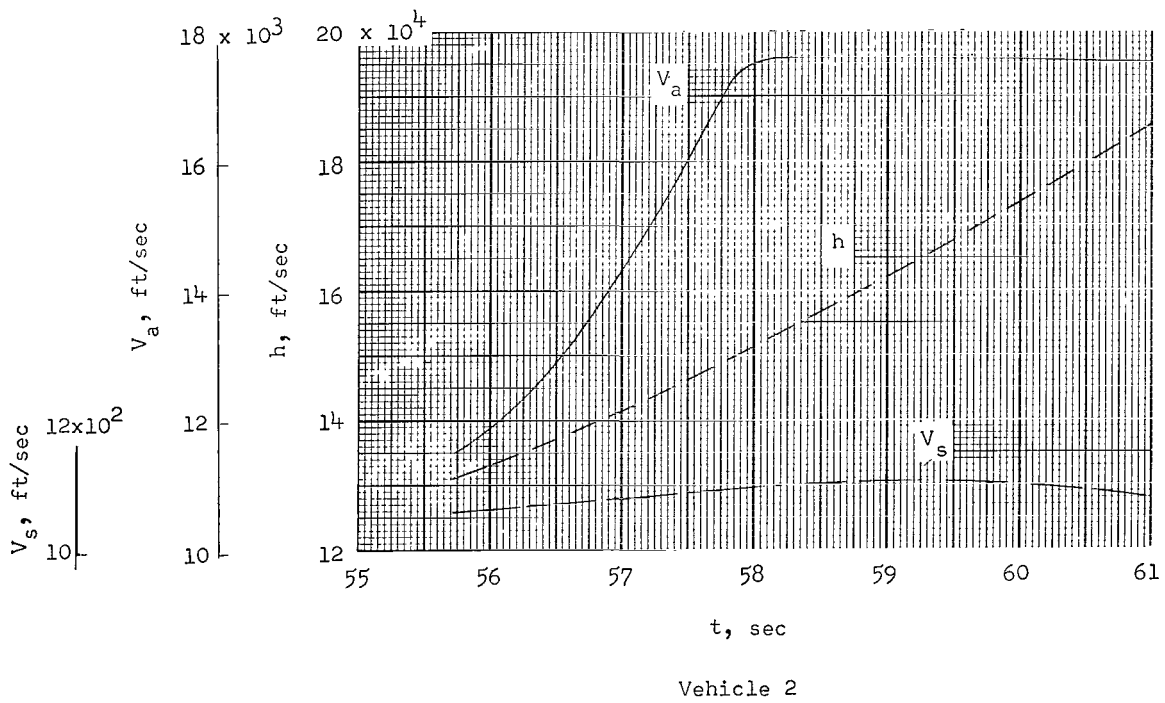
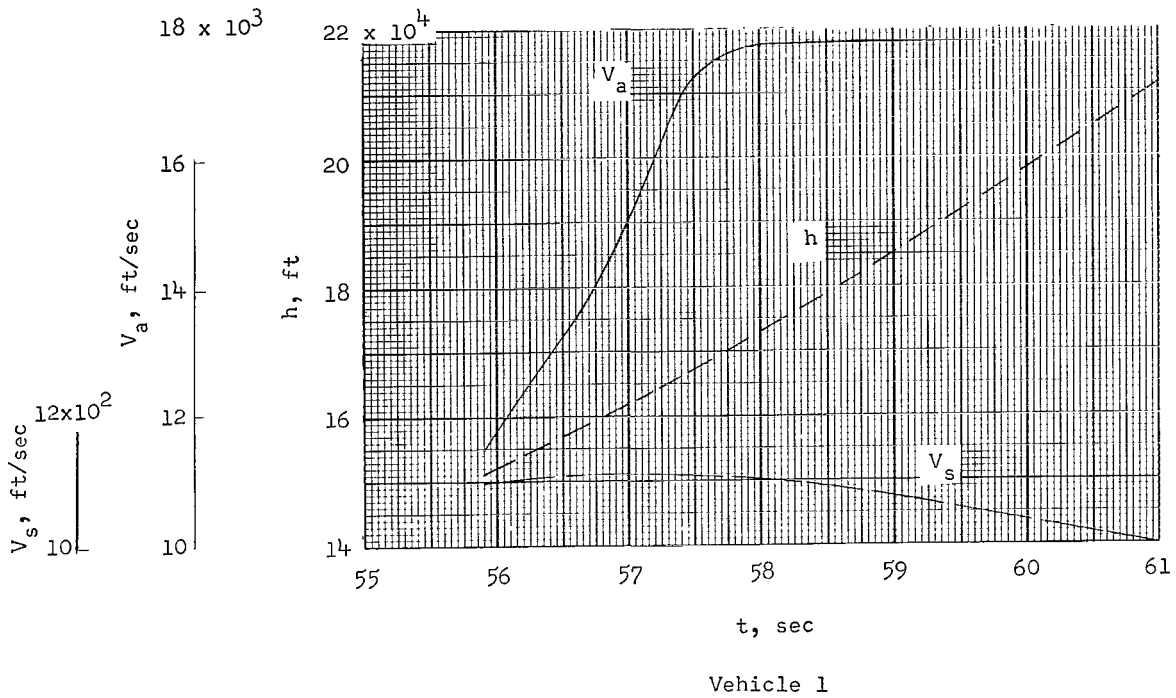
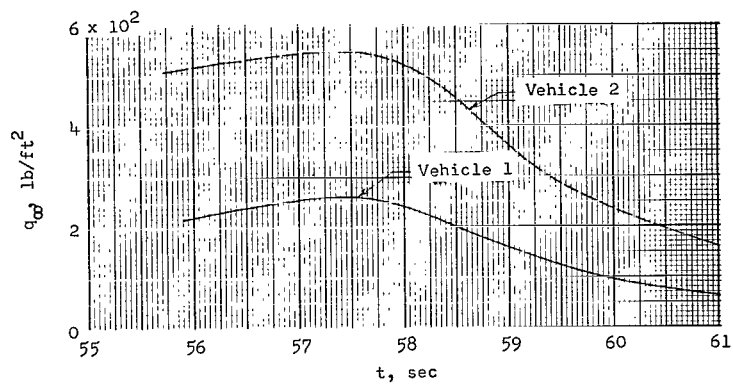


Figure 7.- Variation of rolling velocity with time.

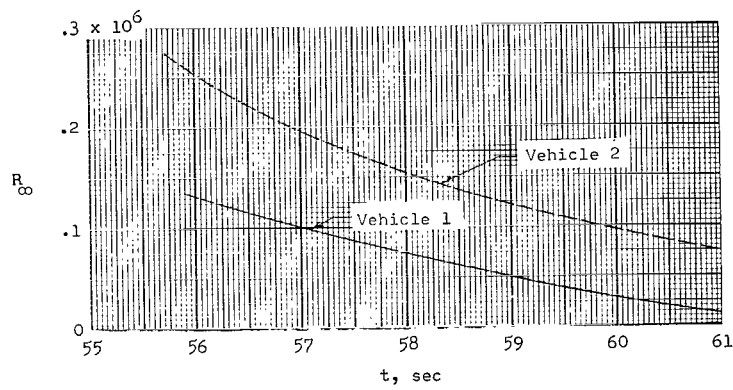


(a) Velocity, altitude, and speed of sound.

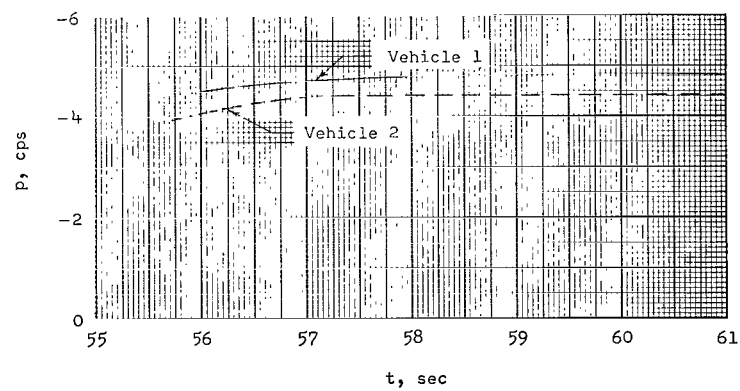
Figure 8.- Vehicle flight parameters throughout simulation region.



(b) Dynamic pressure.



(c) Reynolds number.



(d) Rolling velocity.

Figure 8.- Concluded.

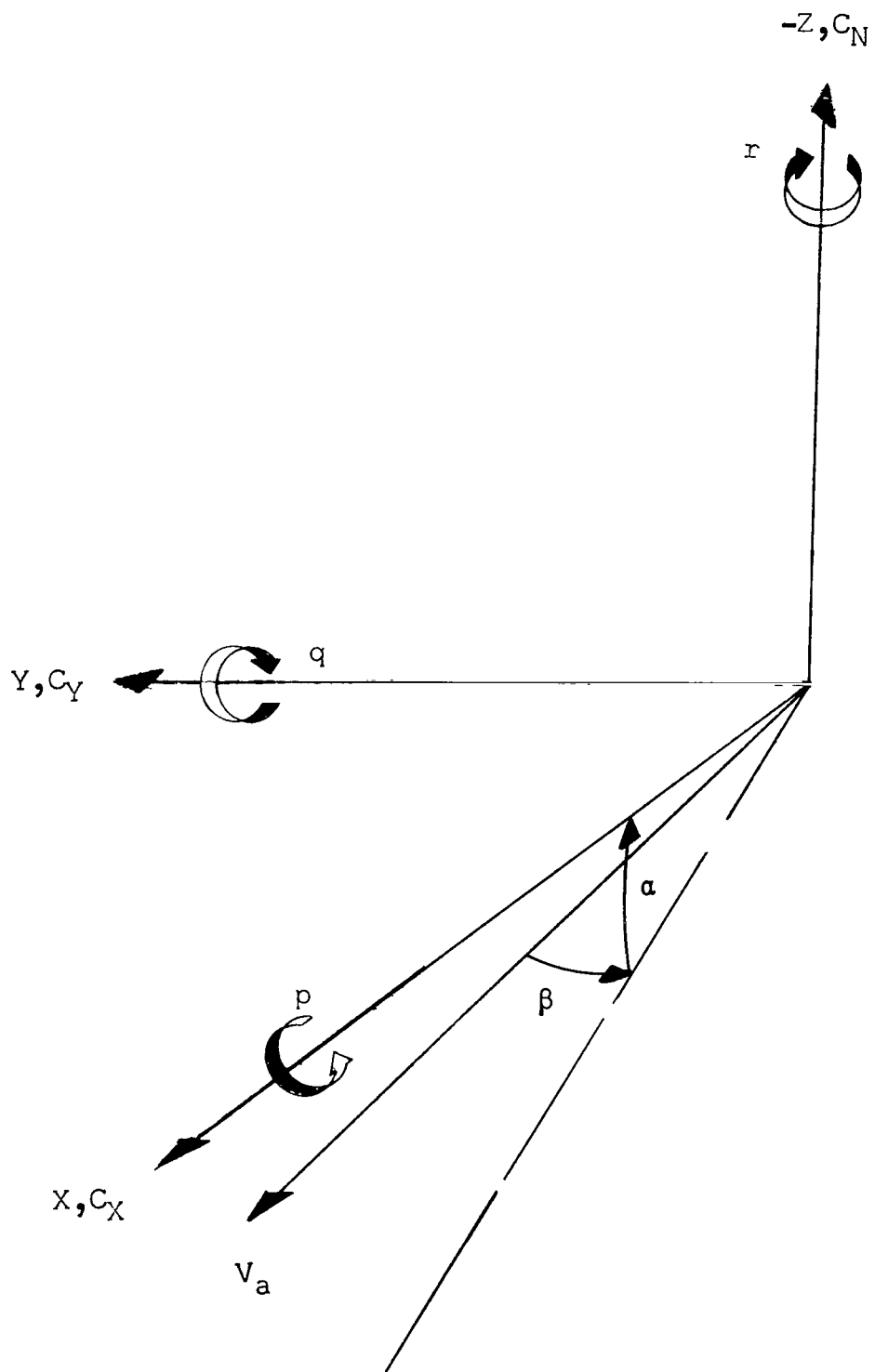


Figure 9.- Body-axis system.





$\alpha = 0^\circ$

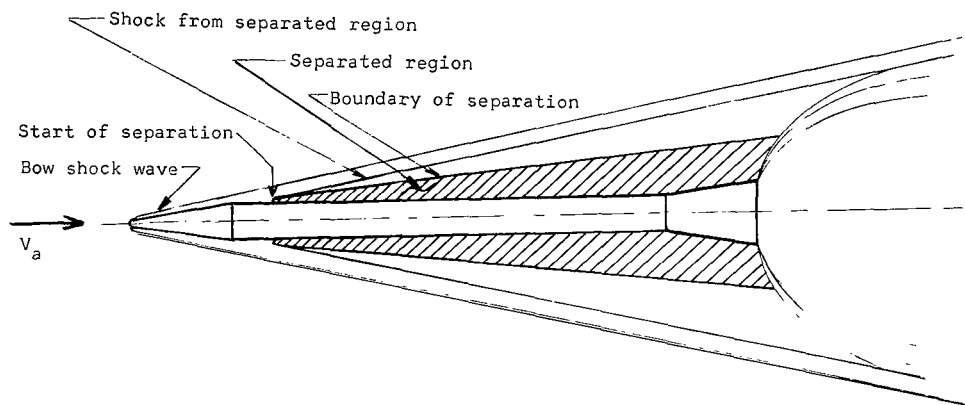


$\alpha = -5^\circ$

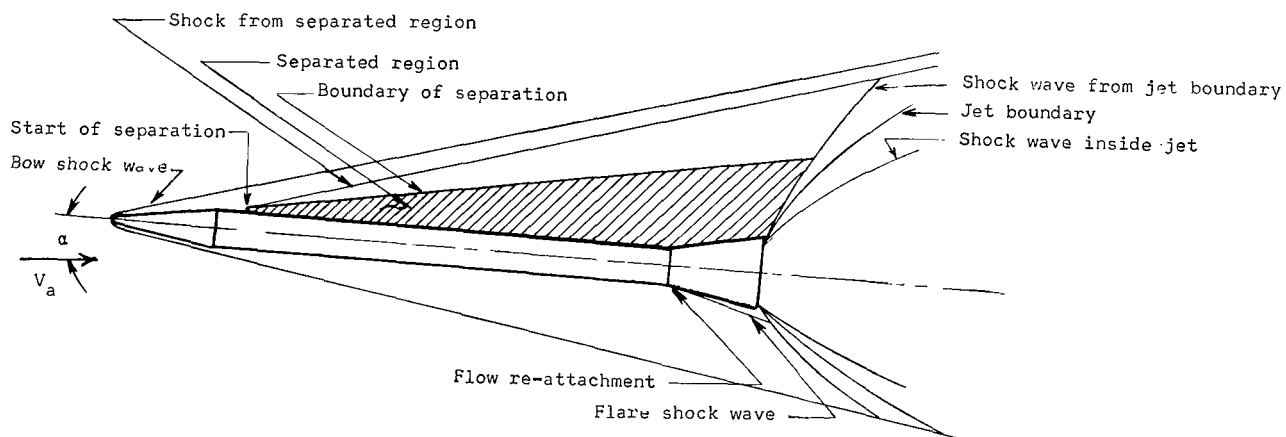
(a) Schlieren photographs.

L-63-4733

Figure 10.- Schlieren photographs and schematic representation of the effect of jet pluming and angle of attack on vehicle boundary layer at  $M = 6.8$  and  $p_j/p_\infty = 200$ .



$\alpha = 0^\circ$



$\alpha = 5^\circ$  (Note that in figure 10(a),  $\alpha = -5^\circ$ )

(b) Schematic representation of the flow-field nomenclature.

Figure 10.- Concluded.

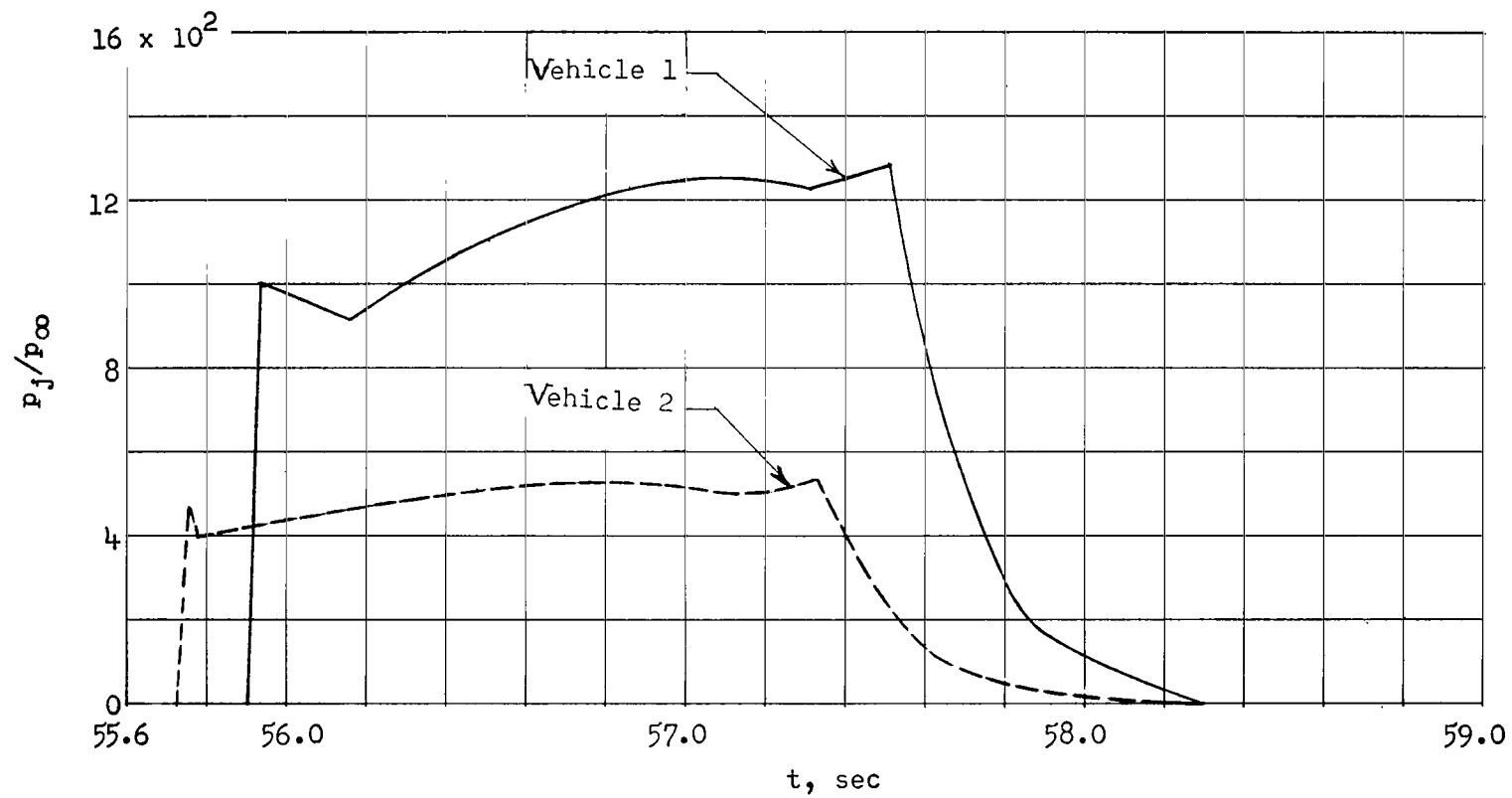


Figure 11.- Variation of fourth-stage jet-exit-to-free-stream-static-pressure ratio with time, based on nominal vacuum rocket-motor performance.

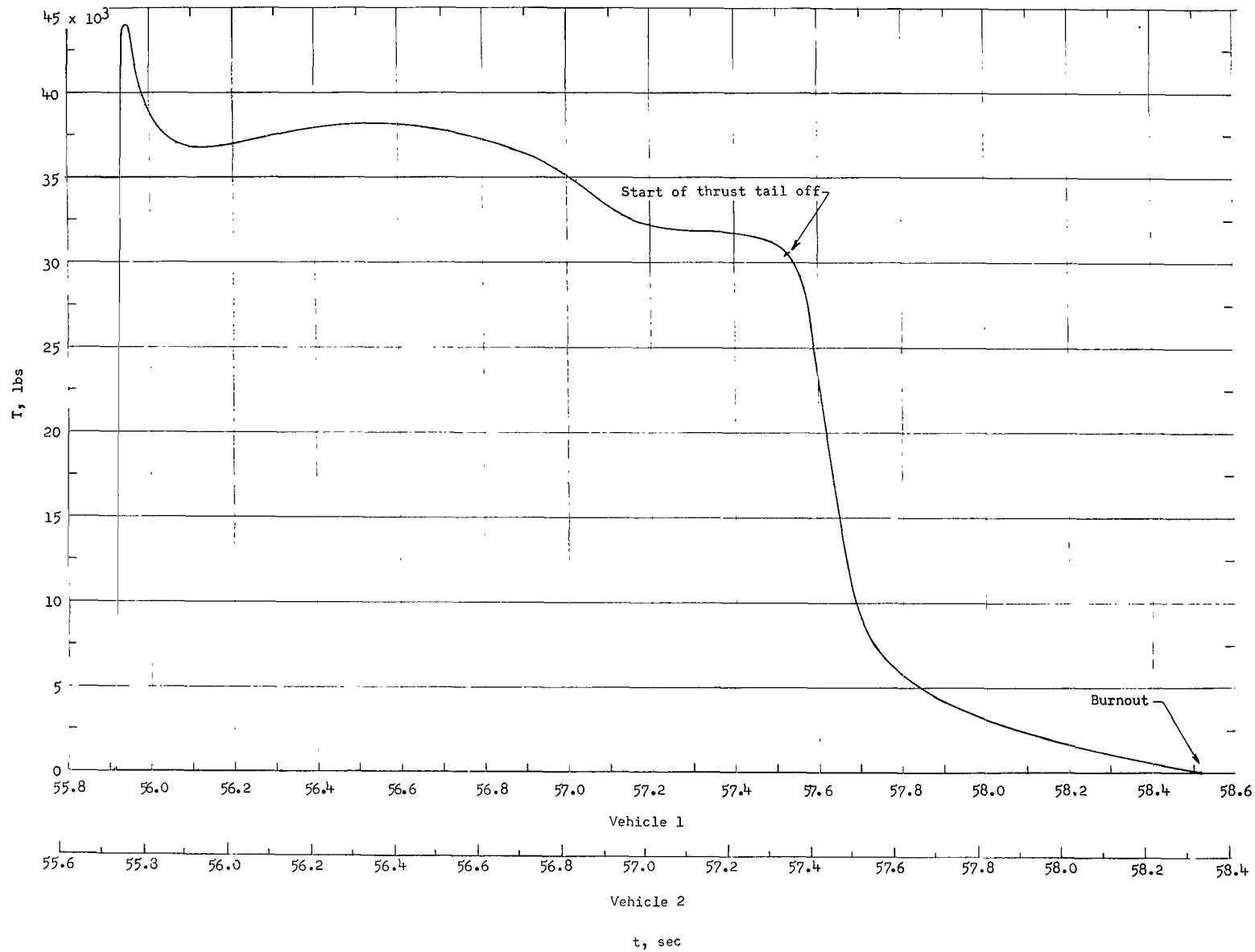
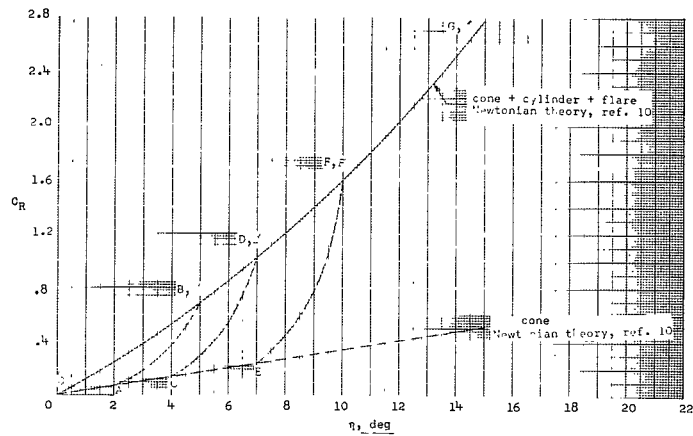
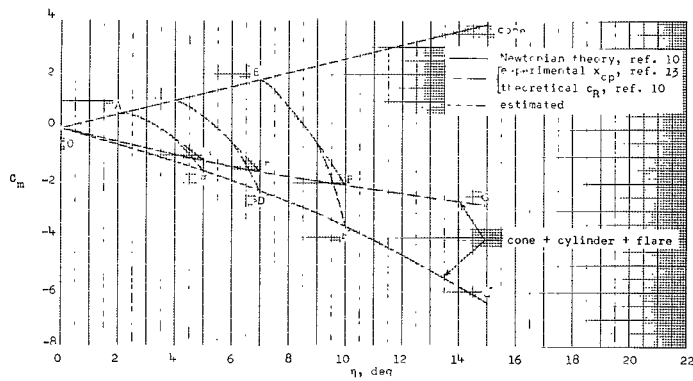


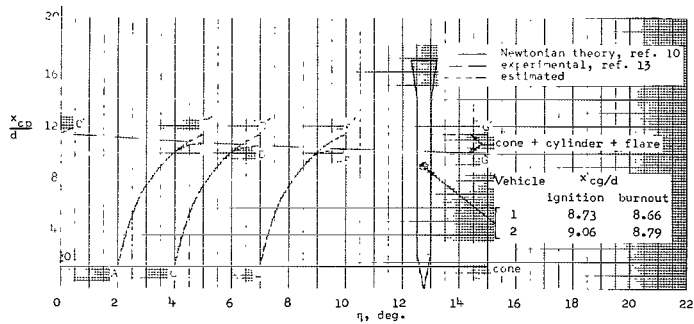
Figure 12.- Variation of nominal vacuum rocket-motor thrust with time for the flight vehicles.



(a) Resultant normal-force coefficient.



(b) Pitching-moment coefficient.



(c) Center of pressure.

Figure 13.- Variations of normal force, center of pressure, and pitching moments with angle of attack employed for simulation analysis.

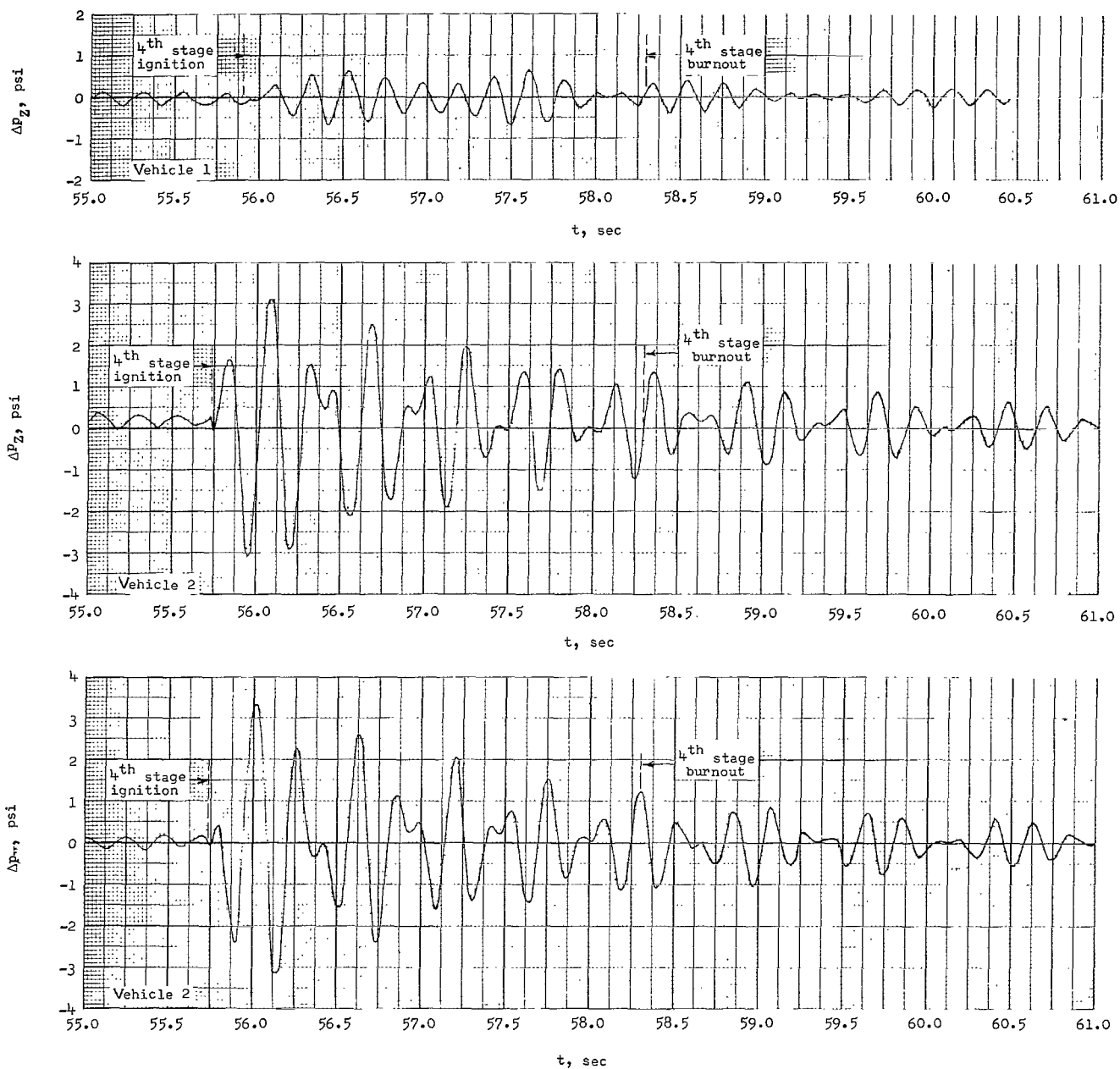
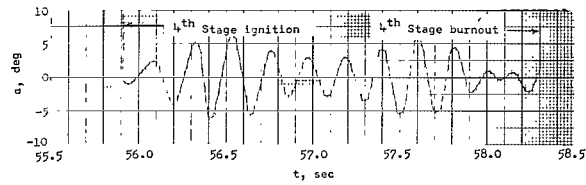
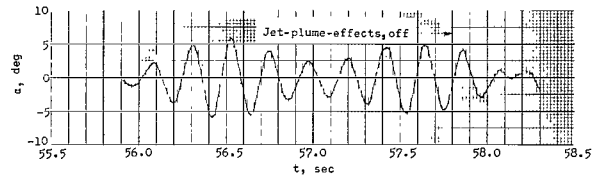


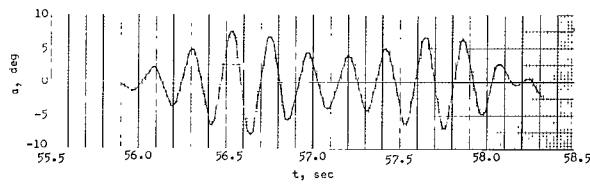
Figure 14.- Variation of measured differential pressures with time.



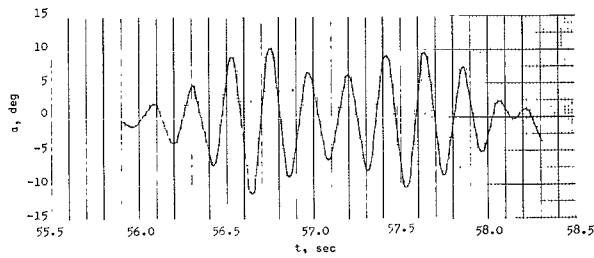
(a) Flight data.



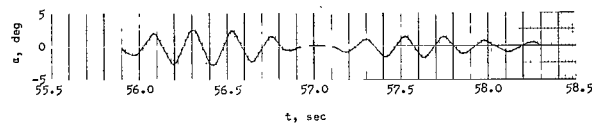
(b) Digital computer,  $C_R$  curve O-A-B'-G' (fig. 13).



(c) Digital computer,  $C_R$  curve O-C-D'-G' (fig. 13).

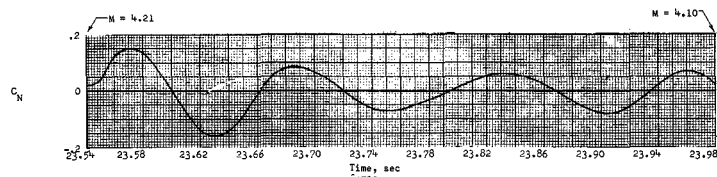


(d) Digital computer,  $C_R$  curve O-E-F'-G' (fig. 13).

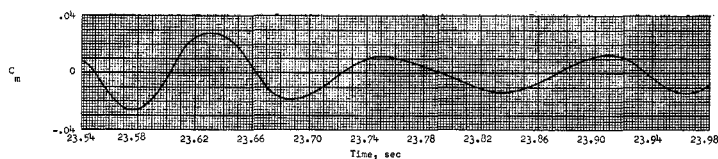


(e) Digital computer,  $C_R$  curve O'-G' (fig. 13).

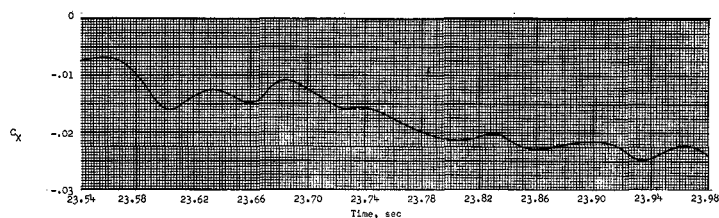
Figure 15.- Comparison of flight and computed incidence angles during the thrusting period for vehicle 1.



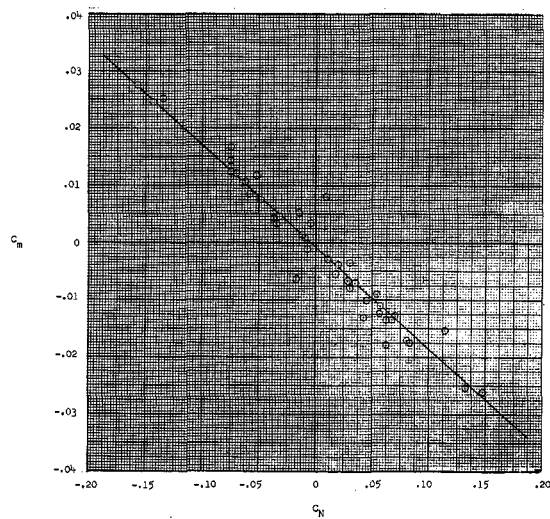
(a) Total normal-force coefficient.



(b) Total pitching-moment coefficient.



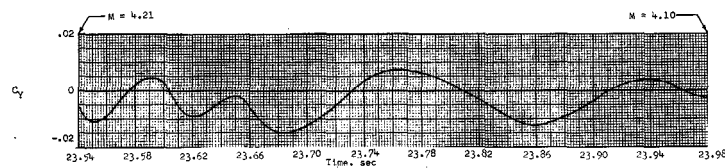
(c) Total axial-force coefficient. Pulse-rocket ignition occurred at 23.52 seconds.



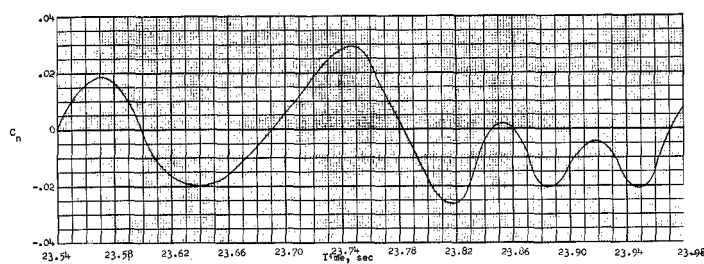
(d) Variation of  $C_m$  with  $C_N$ .

Figure 10.- Time histories of total force and moment coefficients along with cross plots of pitch and yaw coefficients.  $M \approx 4.1$ .

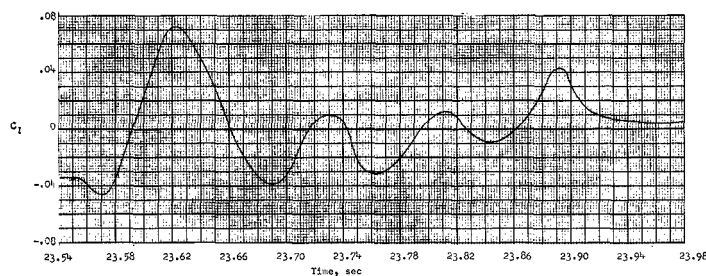




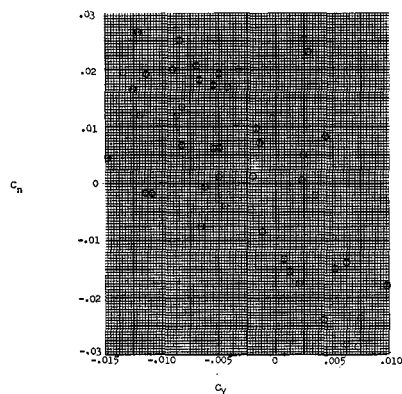
(e) Total side-force coefficient.



(f) Total yawing-moment coefficient.

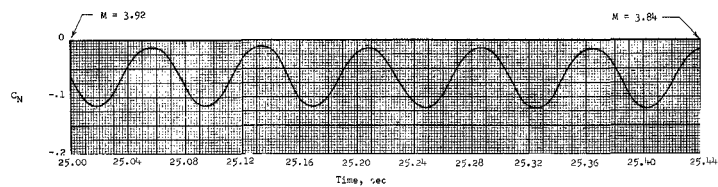


(g) Total rolling-moment coefficient

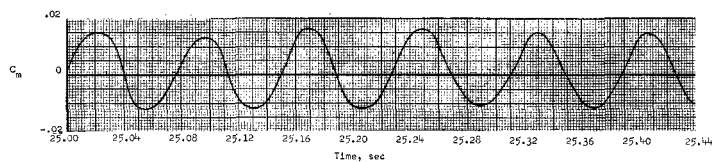


(h) Variation of  $C_n$  with  $C_y$ .

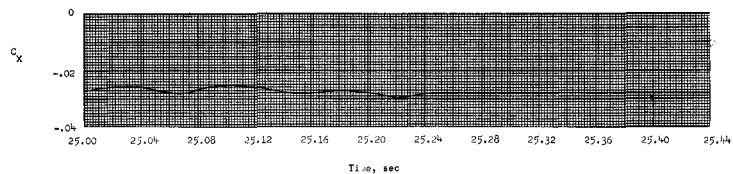
Figure 10.- Concluded.



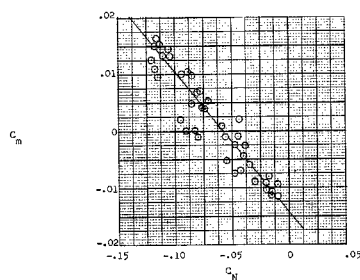
(a) Total normal-force coefficient.



(b) Total pitching-moment coefficient.

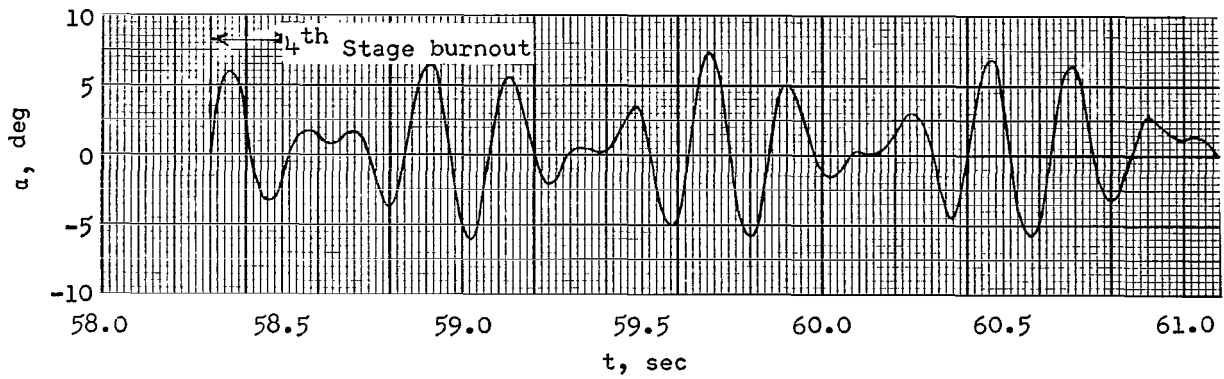


(c) Total axial-force coefficient.

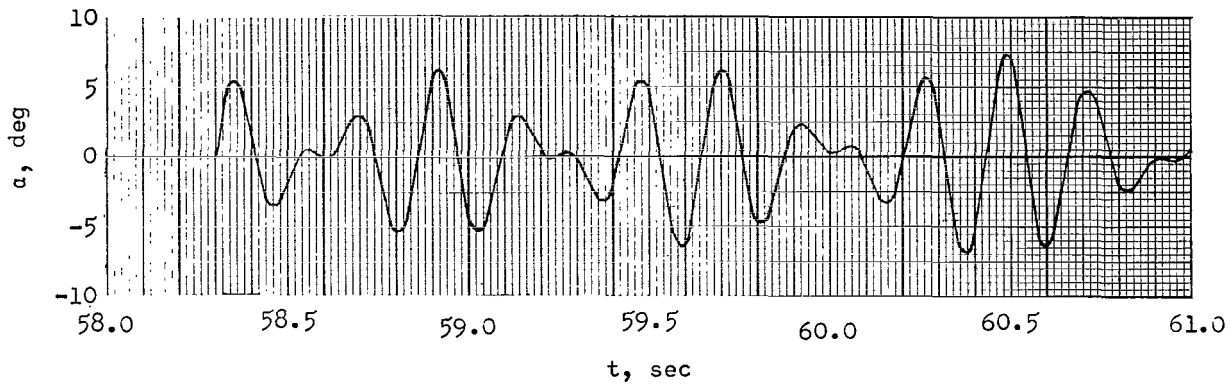


(d) Variation of  $C_m$  with  $C_N$ .

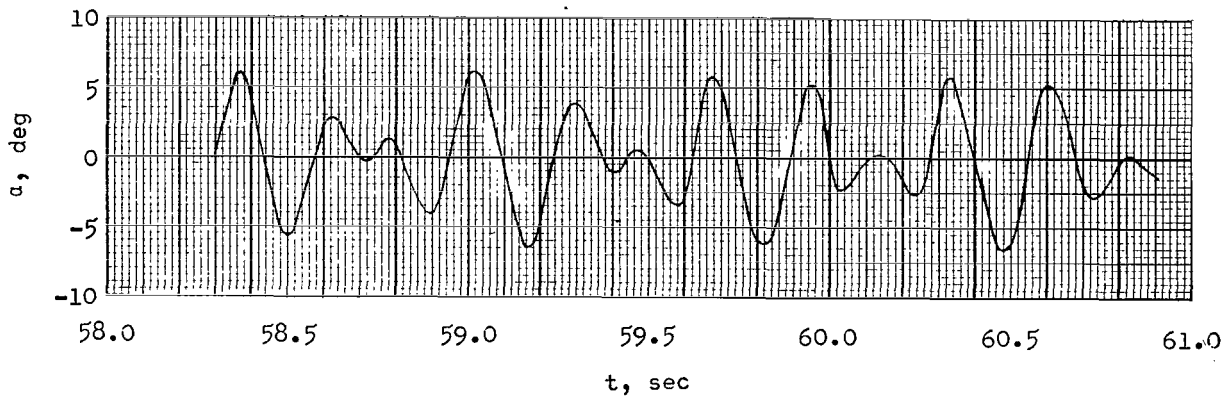
Figure 11.- Time histories of total force and moment coefficients along with cross plots of pitch and yaw coefficient.  $M \approx 3.9$ .



(a) Flight data.

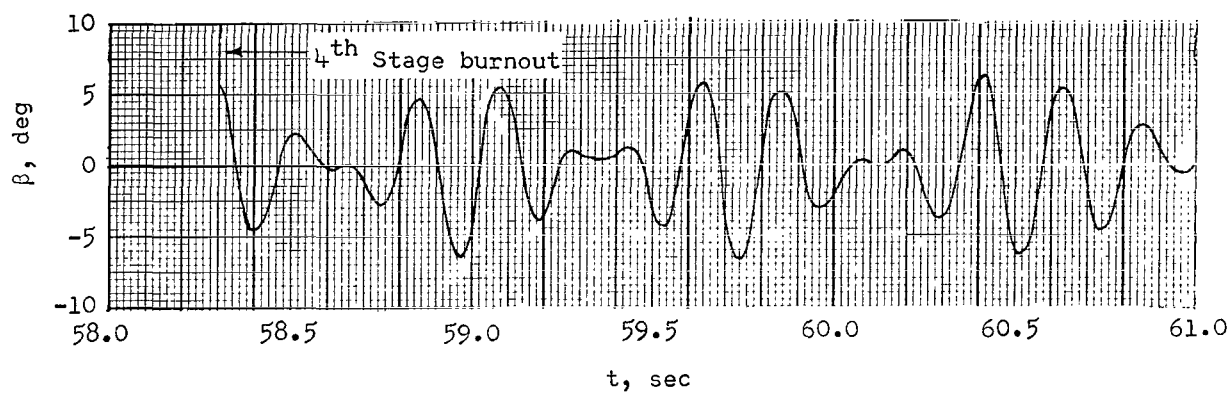


(b) Digital computer. (Curve O'-G', fig. 13.)

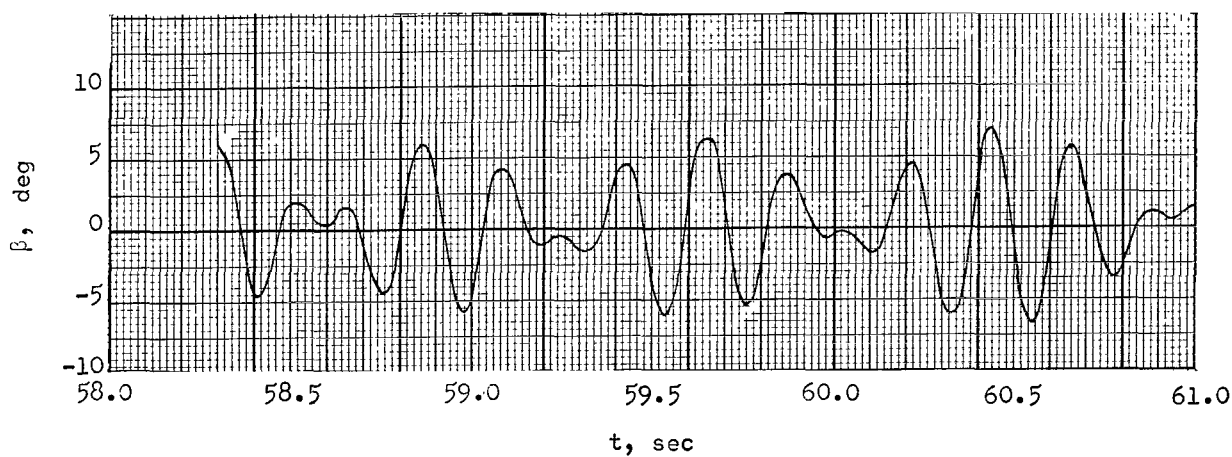


(c) Linearized theory (ref. 10).

Figure 18.- Comparison of flight and computed incidence angles during vehicle 2 coast.



(d) Flight data.



(e) Digital computer. (Curve O'-G' fig. 13.)

Figure 18.- Concluded.